A&A, 711, A243 (2026)
https://doi.org/10.1051/0004-6361/202558481

Astronomy & Astrophysics

Explorations of chaotic diffusions triggered by multiple close encounters in a mean motion resonance of the three-body problem

Xiang Liu[1,2] and Massimiliano Guzzo[2,⋆]

[1] Dalian University of Technology, School of Mathematical Sciences, Dalian District of Ganjingzi City Road 2, 116024, China
[2] Università degli Studi di Padova, Dipartimento di Matematica, Via Trieste 63, 35121 Padova, Italy

Received 9 December 2025 / Accepted 17 April 2026

ABSTRACT

The motion of comets and asteroids for large values of their eccentricity may experience instabilities due to both the action of resonance induced chaos and close encounters with a planet. The spatial circular restricted three-body problem incorporates three characteristic timescales of the phenomenon: a very short one in which the dynamics is dominated by the close encounter with a planet, an intermediate one in which the dynamics is described by a resonant normal form, and a secular one characterized by possible long-term evolution of orbital elements. While extensive literature exists on normal form dynamics, long-term adiabatic evolution, and deep close encounters, less is known about chaotic instability resulting from the accumulation of a sequence of multiple weak close encounters. In this paper, using a combined analysis that leverages the computation of approximate first integrals, of Fast Lyapunov Indicators, of the localization of the gravitational singularities in the phase-space, and of adiabatic theory, we provide examples of chaotic diffusion that, in addition to the crossings of a separatrix, are due to the accumulation of effects of weak close encounters. In particular, we provide examples of how a deeper close encounter may determine the extraction from a main resonance, such as the 1:2 mean motion resonance with Neptune, and the subsequent cascade of close encounters determines a slower chaotic diffusion between the nearby resonances.

Key words. celestial mechanics – minor planets, asteroids: general – planets and satellites: dynamical evolution and stability

1. Introduction

Chaotic instabilities in the motion of asteroids have been extensively studied since the discovery of the Kirkwood gaps in the Solar System's main belt. The crossing of a separatrix within a mean motion resonance (MMR) with a planet is recognized as one of the primary mechanisms of chaos generation (Wisdom 1983; Neishtadt 1987a; Neishtadt & Sidorenko 2004); additional sources of chaos, arising from gravitational interactions, are associated with, for example, three-body or secular resonances and close encounters. In the context of chaos generation within a MMR, adiabatic theory provides the theoretical model to study the coupling between the chaotic motions of the semi-secular resonant normal form variables and the long-term evolution of eccentricity and inclination (see, for example, Wisdom 1983; Neishtadt 1987a; Neishtadt & Sidorenko 2004; Sidorenko 2006; Sidorenko et al. 2014; Milani & Baccili 1998; Efimov et al. 2020; Sidorenko 2024; Ferraz-Mello & Sato 1989; Morbidelli 2002; Nesvorny et al. 2002; Saillenfest et al. 2016; Gallardo 2020; Fenucci et al. 2022; Pan & Gallardo 2025). At high eccentricities, Chirikov diffusion (Chirikov 1979; Morbidelli & Guzzo 1997; Morbidelli 2002) within nearby resonances and close encounters with planets become relevant: in fact, the separatrices of the resonant normal forms overlap (Morbidelli et al. 1995; Morbidelli 2002) and, when the planetary orbits are crossed, close encounters and collisions become possible.

Some studies have modeled the effect of an individual close encounter, which may induce a sharp change in the orbital elements, potentially leading to extraction from a MMR (Öpik 1976; Valsecchi 2002; Guzzo 2024). Other studies have incorporated the effects of close encounters into averaged normal form dynamics to the maximum extent possible (for example, in Lidov & Ziglin 1974; Ferraz-Mello & Sato 1989; Beauge 1994; Morbidelli et al. 1995; Thomas 1998; Gronchi & Milani 1998; Milani & Baccili 1998; Roig et al. 1998; Morbidelli 2002; Nesvorny & Roig 2000, 2001; Nesvorny et al. 2002; Sidorenko 2006; Ferraz-Mello 2007; Gronchi & Tardioli 2012; Sidorenko et al. 2014; Saillenfest et al. 2016; Maró & Gronchi 2018; Efimov et al. 2020; Gallardo 2020; Pan & Gallardo 2025; Fenucci et al. 2022; Sidorenko 2024; Liu & Guzzo 2025). In fact, while the averaged normal form may be not valid to describe the effect of an individual deep close encounter, it can be used to study the evolution of the orbital elements of the asteroid (or comet) in cases in which the minimum distance between the asteroid and the planet, attained during a resonant cycle, may progressively decrease. When the close encounter is sufficiently deep, it may produce sharp variations in the averaged Hamiltonian, and extract the small body, P, from the given MMR. In the planar problem, the analysis of close encounters in a MMR is simplified by specific features (Morbidelli et al. 1995; Thomas 1998; Nesvorny et al. 2002; Liu & Guzzo 2025). In particular, the normal form Hamiltonian of a $p:q$ MMR is completely integrable (apart from a remainder that is initially neglected), since it depends on the angles only through the critical angle of the resonance[1] $\sigma = q\lambda - p\lambda_1 - (q-p)\varpi$. Correspondingly, for the

[1] We denote with $(a, e, i, M, \omega, \Omega)$ the orbital elements of the massless body, with ϖ the longitude of perihelion, and with λ and λ_1 the true longitudes of the massless body and of the secondary body.

⋆ Corresponding author: guzzo@math.unipd.it

planar problem the quantity

$$N_{pl} = \sqrt{a}[p - q\sqrt{1-e^2}] \quad (1)$$

is a first integral, and for every given value of N_{pl} the dynamics have a phase-portrait that can be represented in the plane of the resonant variables S, σ (S is the conjugate action to σ; see for example Henrard et al. 1983; Lemaitre 1984; Winter & Murray 1997a,b; Morbidelli 2002); the integrable Hamiltonian representing the MMR dynamics will hereafter be called the averaged Hamiltonian. The action N_{pl} is the crucial parameter to classify the phase-portraits of the averaged Hamiltonian of the planar problem (see, for example, Henrard et al. 1983; Lemaitre 1984; Beauge 1994; Morbidelli 2002), and its value indicates also the possibility of collisions with the planet, P_1 (see Beauge 1994; Thomas 1998; Morbidelli 2002). In particular, there is a critical value of N_{pl}, which we denote by N_c hereafter, such that for values of $N_{pl} > N_c$ we have a curve of the resonant phase-plane, hereafter called singular set, where a collision of P with P_1 is possible (Beauge 1994; Morbidelli et al. 1995; Thomas 1998; Liu & Guzzo 2025). The singular sets play a crucial role in the generation of complex orbits of the planar problem with essentially two mechanisms. In the first one (Morbidelli et al. 1995; Thomas 1998), following the level curves of the resonant phase-portrait an orbit may hit the singular set and P experiences a deep close encounter with P_1. During the deep close encounter, the averaging method is not effective, and correspondingly N_{pl} and the averaged Hamiltonian cease to be first integrals and may undergo large variations. Also, by following the level curves of the resonant phase-portrait the orbit approaches the singular set at a relatively large distance corresponding to a weak encounter of P with P_1 (see for example, Liu & Guzzo 2025). During these weak close encounters we detected tiny variations in N_{pl} and in the value of the averaged Hamiltonian, which nevertheless may increase the amplitude of resonant librations and decrease the minimum distance attained at subsequent close encounters. A sufficiently deep close encounter terminates the validity of the resonant normal form approximation and may extract the body, P, from the resonance.

The analysis of the singularities of the averaged Hamiltonian in the spatial CRTBP is complicated by the more complex geometry of close encounters due to the higher dimensionality (Nesvorny et al. 2002; Saillenfest et al. 2016; Fenucci et al. 2022; Sidorenko 2024). In the spatial case, the flow of the averaged Hamiltonian still has a first integral:

$$N = \sqrt{a}\left(p - q\sqrt{1-e^2}\cos(i)\right), \quad (2)$$

but is not integrable since it depends on two angles, and it can exhibit chaotic motions generated by the crossing of a separatrix of the averaged Hamiltonian (Wisdom 1983; Neishtadt 1987a; Neishtadt & Sidorenko 2004). In the spatial case, we have two relevant phase-planes: a plane of the semi-secular variables S, σ, where σ is the critical angle of the resonance and S its conjugate action, and a plane of variables A, α, representing only secular evolution (see Eq. (4)). The chaotic diffusion of the secular variables A, α can determine the secular instability of the orbit of P, which has been effectively studied using the theory of adiabatic invariants (Wisdom 1983; Neishtadt 1987a; Neishtadt & Sidorenko 2004) applied to the averaged Hamiltonian. Another source of slow secular instability in external MMRs has been related to sequences of close encounters with a planet. For example, in Morbidelli (1997), the ejection of comets from the 2:3 MMR was related to the combination of chaotic diffusion and collisional "kicks". In this paper we analyze in detail for the spatial CRTBP how the crossing of a region of the resonant plane S, σ where close encounters with a planet occur results in a combination of adiabatic chaos, occurring with conservation of the averaged Hamiltonian $\widehat{H}$ and of the action N, and diffusion of these quantities. In fact, we see that between two consecutive clusters of close encounters, the averaging is effective, showing a good conservation of $\widehat{H}$ and N. Correspondingly, far from close encounters the dynamics is studied using the theory of adiabatic invariants, with a characterization of the projection of the averaged orbits in the semi-secular plane S, σ and the secular plane A, α. At close encounters, we observe almost step-wise jumps in $\widehat{H}$ and N, possibly determining the extraction from the MMR. In fact, when the close encounter is sufficiently deep, it can alone determine the extraction from the MMR. But, for moderate close encounters the step-wise jumps of $\widehat{H}$ and N are qualitatively similar to the ones modeled for Arnold diffusion in Guzzo et al. (2020). In particular, when the examined orbits arrive just outside the external separatrix that delimits the resonance, they begin a sequence of moderate close encounters that can lead them toward other nearby resonances, as for the Chirikov diffusion. In more detail, the analog of the singular set (which was the most relevant geometric object in the planar case) may be just a point in the semi-secular phase-plane S, σ and its role is replaced by a curve of values of the plane S, σ (for given values of A, N, α characterized by a possible small distance from P_1; see the definition of minimum resonant distance (MRD) given in Section 2). A neighborhood of this curve represents the place of the plane S, σ where resonant motions (regular or chaotic) may undergo a close encounter with the planet, determining a jump in the values of $\widehat{H}$ and N, possibly extracting P from the region of resonant librations. Following this event, P may enter a chaotic region characterized by many crossings with the region of small MRD, determining a diffusion toward a nearby MMR. This process is similar to the Chirikov diffusion between nearby overlapping resonances, but is triggered by close encounters: the diffusion is due to the accumulation of the sharp variations of N and of the averaged Hamiltonian occurring at close encounters of P with P_1. At the same time, chaotic diffusion is observed for the variables A, α.

This article is structured as follows. In Section 2, we recall the definition of the MMR resonant normal form and the semi-secular and secular phase planes, and we provide the definition of singular sets and lines of small MRD in the semi-secular plane. In Section 3 we provide examples of regular and chaotic motions: we distinguish the case of N much smaller than the critical value N_c (for which collisions are not possible within the MMR); N close to N_c; N much larger than N_c, and we highlight the role of sequences of close encounters for producing chaotic diffusion. All the examples are provided for the sample external 1:2 MMR. In the appendix we provide some details about the averaging transformation, the computation of the averaged Hamiltonian, the adiabatic invariants, the definition of Fast Lyapunov Indicators, and the representation of the singular sets. Conclusions are provided in Section 4.

2. The averaged Hamiltonian, the singular set, and the line of MRD

Let us consider the Hamiltonian of the spatial circular restricted three-body problem represented in the heliocentric reference frame,

$$H := -\frac{1}{2\Lambda^2} + n_1\Lambda_1 + \varepsilon H_1(\Lambda, \Phi, \Gamma, \lambda, \varphi, \gamma, \lambda_1), \tag{3}$$

using the modified Delaunay variables,

$$\begin{aligned} \Lambda &= \sqrt{a}, & \lambda &= M + \omega + \Omega, \\ \Phi &= \sqrt{a}(1 - \sqrt{1-e^2}), & \varphi &= -(\omega + \Omega), \\ \Gamma &= \sqrt{a}\sqrt{1-e^2}(1 - \cos(i)), & \gamma &= -\Omega, \end{aligned}$$

where $(a, e, i, M, \omega, \Omega)$ are the orbital elements of the massless body P, λ_1 denotes the longitude of the planet P_1 and Λ_1 is its conjugate action (we assume that the mass of the primary body P_0, is $m_0 = 1$; the mass of the secondary body P_1, is ε; $\|P_0 - P_1\| = 1$; $G = 1$; and n_1 denotes the frequency of the mean motion of P_1). As usual, we introduce action-angle variables $S, A, N, \Theta, \sigma, \alpha, \nu, \theta$ adapted to the study of a $p : q$ external MMR of order $q - p = 1$ (see for example Morbidelli 2002; Milani & Baccili 1998):

$$\begin{pmatrix} \sigma \\ \alpha \\ \nu \\ \theta \end{pmatrix} = \begin{pmatrix} q & q-p & 0 & -p \\ 0 & 1 & -1 & 0 \\ -1 & 0 & 0 & 0 \\ 0 & 0 & 0 & 1 \end{pmatrix} \begin{pmatrix} \lambda \\ \varphi \\ \gamma \\ \lambda_1 \end{pmatrix} \tag{4a}$$

$$\begin{pmatrix} S \\ A \\ N \\ \Theta \end{pmatrix} = \begin{pmatrix} 0 & 1 & 1 & 0 \\ 0 & 0 & p-q & 0 \\ p-q & q & q & 0 \\ 0 & p & p & 1 \end{pmatrix} \begin{pmatrix} \Lambda \\ \Phi \\ \Gamma \\ \Lambda_1 \end{pmatrix}, \tag{4b}$$

where in particular $\theta = \lambda_1$ and $\nu = -\lambda$ are fast angles, $\sigma = q\lambda - p\lambda_1 - (q-p)(\Omega + \omega)$ is the critical angle of the resonance, and $\alpha = -\omega$ is a secular angle. In these variables, the Hamiltonian of the problem is represented as the sum of the integrable part,

$$\widehat{H}_0 := -\frac{1}{2(qS - N)^2} + n_1(-pS + \Theta), \tag{5}$$

and of the perturbing function, $\varepsilon\widehat{H}_1$, dependent on $S, A, N, \sigma, \alpha, \nu + \theta$, which is expressed by the Fourier expansion,

$$\begin{aligned} \widehat{H}_1 :=& c_0(S, A, N, \sigma, \alpha) + \sum_{k=1}^{\infty} c_k(S, A, N, \sigma, \alpha)\cos(k(\nu + \theta)) \\ &+ \sum_{k=1}^{\infty} s_k(S, A, N, \sigma, \alpha)\sin(k(\nu + \theta)), \end{aligned} \tag{6}$$

with

$$c_0 := \frac{1}{2\pi}\int_0^{2\pi} \widehat{H}_1(S, A, N, \sigma, \alpha, \nu + \theta)\mathrm{d}(\nu + \theta) \tag{7}$$

and, for $k \geq 1$,

$$c_k := \frac{1}{\pi}\int_0^{2\pi} \widehat{H}_1(S, A, N, \sigma, \alpha, \nu + \theta)\cos[k(\nu + \theta)]\mathrm{d}(\nu + \theta) \tag{8}$$

$$s_k := \frac{1}{\pi}\int_0^{2\pi} \widehat{H}_1(S, A, N, \sigma, \alpha, \nu + \theta)\sin[k(\nu + \theta)]\mathrm{d}(\nu + \theta). \tag{9}$$

We remark that a key element of the approach included in the present paper is the canonical transformation in Eqs. (4) and (4b) that makes the Hamiltonian to depend on the fast angles ν and θ only through their sum $\nu + \theta$ (see Appendix A for details).

From Eqs. (5) and (6) one defines the averaged Hamiltonian:

$$\widehat{H} = \widehat{H}_0(S, N, \Theta) + \varepsilon c_0(S, A, N, \sigma, \alpha), \tag{10}$$

whose dynamics is related to the dynamics of the three-body problem only in a domain of the phase-space in which a close-to-the-identity canonical transformation, ψ (hereafter called averaging transformation), conjugates the original Hamiltonian to the resonant normal form,

$$H^{Res} := \widehat{H}(S, A, N, \sigma, \alpha) + \varepsilon^2\widehat{R}(S, A, N, \sigma, \alpha, \nu + \theta), \tag{11}$$

where the dependence on the fast angle, $\nu + \theta$, is relegated to the remainder, $\varepsilon^2\widehat{R}$ (see Appendix B for details about the definition and computation of the averaging transformation, ψ). In such a domain, the dynamics in the MMR is approximated with the dynamics of the averaged Hamiltonian, $\widehat{H}$, which is obtained from the resonant normal form (11) by neglecting the remainder, $\varepsilon^2\widehat{R}$.

The analysis of the dynamics of the averaged Hamiltonian has been done in the literature by noticing that N, Θ are first integrals for the Hamiltonian flow of $\widehat{H}$, and therefore one proceeds by studying the dynamics in the reduced phase-space of the variables S, A, σ, α. Moreover, the conjugate variables A, α have slow variation, since their time derivatives (obtained from the Hamilton equations of $\widehat{H}$) are proportional to ε, while the conjugate variables S, σ have faster variation in the domain of the MMR (typically they evolve on timescales on the order of $1/\sqrt{\varepsilon}$). Therefore, the phase-portraits of $\widehat{H}$ obtained for fixed N, A, α provide a first approximation of the dynamics that is valid for times much smaller than $1/\varepsilon$. For longer times the theory of adiabatic invariants has been used to study the secular evolution of the variables A, α, predicting the existence of regular as well as of chaotic motions (Wisdom 1983; Neishtadt 1987a; Neishtadt & Sidorenko 2004; Sidorenko 2006; Sidorenko et al. 2014; Efimov et al. 2020; Sidorenko 2024; Saillenfest et al. 2016; Gallardo 2020; Fenucci et al. 2022). For $N > N_c$ (actually, also for $N \leq N_c$ whenever $N \sim N_c$) the possibility of close encounters adds an additional source of instability, since the conservation of the averaged Hamiltonian may be broken, enlarging the possibility of generation of complex orbits and chaotic diffusion. Therefore, when analyzing the resonant dynamics characterized by multiple close encounters, a crucial question is related to the domain where the conjugation of $\widehat{H}_0 + \varepsilon\widehat{H}_1$ to its normal form Hamiltonian, H^{Res}, is not defined due to the singularities of the perturbing function.

Two prerequisites for the existence of the averaging transformation, ψ, are: the regularity of the Fourier expansion (6); and $\varepsilon\widehat{H}_1$ being a perturbation of $\widehat{H}_0$. Neither of these requirements is satisfied in a specific domain of the reduced phase-space variables S, A, N, σ, α due to the gravitational singularities of the perturbation. In fact, the integrands appearing in Eqs. (7), (8), and (9) are singular when they are computed on $S, A, N, \sigma, \alpha, \nu, \theta$ in the collision set:

$$C = \{\xi = (S, A, N, \sigma, \alpha, \nu, \theta) : \mathbf{r}_{|\xi} = (\cos\theta, \sin\theta, 0)\}, \tag{12}$$

which contains the states of P with a radius vector corresponding to a collision of P with P_1 ($\mathbf{r}$ denotes the radius vector $P - P_0$ parameterized by ξ). As a consequence, the Fourier coefficients c_k, s_k (or their derivatives) are not defined on the set of the reduced phase-space variables,

$$\mathcal{S} = \{(S, A, N, \sigma, \alpha) : \exists\, \nu, \theta \text{ with } (S, A, N, \sigma, \alpha, \nu, \theta) \in C\},$$

which we call the singular set.

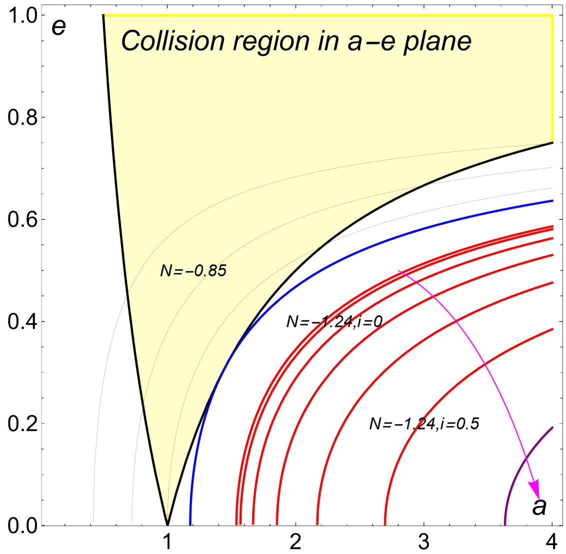

Fig. 1. Level curves of N defined in Eq. (2) for the 1:2 MMR, for different values of the inclination, i. The yellow region represents the solutions to Eq. (15). The blue and gray curves are level curves of N for $i = 0$. All the red curves are level curves of $N = -1.24$ with the inclination increasing from $i = 0$ to $i = 34.4°$ (the pink curve denotes the direction in which the inclination increases). For a fixed value of N, the level curves move far away from the collision region as the value of inclination increases. For the 1 : 2 MMR the critical value is $N_c \simeq -1.08524$.

2.1. Characterization of the collision and singular sets

In this section, we characterize the collision set, C, and the singular set, $\mathcal{S}$, in the space of the resonant action-angle variables $(S, A, N, \sigma, \alpha, \nu, \theta)$. This discussion is presented here for the external $p : q$ MMRs of order 1, i.e., $q = p + 1$.

We first consider the collision set, containing all the states of P determined by the values $S, N, A, \sigma, \alpha, \nu, \theta$ for which the corresponding radius vector, $\mathbf{r} = P - P_0$, satisfies

$$\mathbf{r} = (\cos\theta, \sin\theta, 0). \tag{13}$$

Since Eq. (13) is easily represented explicitly using the orbital elements $a, e, i, f, \omega, \Omega$, we first represent the values of the actions,

$$\begin{aligned} S &= \sqrt{a}\left[1 - \sqrt{1-e^2}\cos(i)\right] \\ A &= (p-q)\sqrt{a}\sqrt{1-e^2}\,[1-\cos(i)] \\ N &= \sqrt{a}\left[p - q\sqrt{1-e^2}\cos(i)\right], \end{aligned} \tag{14}$$

which identify the values of a, e, i. For simplicity, we only considered values of the actions corresponding to $a > 1$ (external resonances), $e \in (0, 1)$ (eccentric orbits), and $i \in (0, \pi/2)$ (inclined prograde orbits):

(i) For a given resonance, there exists a critical value, N_c, which is negative and such that for $N < N_c$ the singular and the collision sets are empty (Beauge 1994; Morbidelli et al. 1995; Thomas 1998; Liu & Guzzo 2025, see also Fig. 1).

(ii) Then, we consider $N \in (N_c, 0)$. A necessary condition for $(S, A, N, \sigma, \alpha) \in \mathcal{S}$ is that S, A, N, α identify a Keplerian ellipse with orbital parameters a, e, i, ω that ensure the intersection of the ellipse with the orbit of P_1 (the case of tangent orbits is not considered for simplicity). Therefore, S, A, N must determine values of a, e, i with

$$a(1-e) < 1 < a(1+e). \tag{15}$$

For $a > 1$, Eq. (15) becomes

$$a(1-e) < 1. \tag{16}$$

With some basic algebraic manipulations of Eq. (14), one recognizes that condition (16) is satisfied if (A, S) belongs to a two-dimensional subset of $\mathbb{R}^2$ (see Appendix F).

(iii) After the actions S, A, N have been chosen so that a, e, i satisfy condition (16) and $i \in (0, \pi/2)$, we have to characterize the values of the angles that indeed, for these values of a, e, i, provide a solution to Eq. (13). Since the inclined orbits of P may cross the orbit of P_1 only at the nodes, we have a solution to Eq. (13) corresponding to a collision at the ascending node if $f, \omega, \Omega, \theta$ satisfy the system

$$\frac{a(1-e^2)}{1+e\cos(f)} = 1 \tag{17a}$$

$$\omega + f = 0 \tag{17b}$$

$$\theta - \Omega = 0, \tag{17c}$$

and a similar system for the collision at the descending node. Eq. (17a) has two solutions, $f = f_*^j(S, A, N)$, $j = 1, 2$, which correspond to two values for the mean anomaly, $M = M_*^j(S, A, N)$. Therefore, $f, \omega, \Omega, \theta$ solve Eqs. (17a), (17b), (17c) providing a collision at the ascending node (a similar system holds for the descending node) if

$$f = f_*^j(S, A, N), \quad \omega = -f_*^j(S, A, N), \quad \Omega = \theta. \tag{18}$$

By inverting the transformation (4a) and performing a few algebraic simplifications, the solutions (18) are mapped to

$$\begin{pmatrix} \sigma \\ \alpha \\ \nu + \theta \end{pmatrix} = \begin{pmatrix} q & p & -p \\ 0 & -1 & 0 \\ -1 & -1 & 1 \end{pmatrix} \begin{pmatrix} M_*^j(S, A, N) \\ -f_*^j(S, A, N) \\ 0 \end{pmatrix}. \tag{19}$$

Therefore, when S, A, N determine a, e, i satisfying Eq. (15) with $i \in (0, \pi/2)$, there exists a discrete set of functions, $\hat{\alpha}(S, A, N), \hat{\sigma}(S, A, N), \hat{\nu}(S, A, N)$, such that S, A, N, σ, α with

$$\begin{aligned} \sigma &= \hat{\sigma}(S, A, N) \\ \alpha &= \hat{\alpha}(S, A, N) \end{aligned} \tag{20}$$

is in the singular set, and if moreover

$$\nu + \theta = \hat{\nu}(S, N, A), \tag{21}$$

$(S, A, N, \sigma, \alpha, \nu, \theta)$ is in the collision set.

From the parameterizations (20), we obtain that the intersection of the singular set with the four-dimensional reduced phase-space of variables (S, A, σ, α) for given values of $N > N_c$ is a two-dimensional set. Moreover, for fixed values of the slow variables A, α, the intersection of the singular sets, $\mathcal{S}$, with the plane of the resonant variables (S, σ), when non-empty, typically consists of isolated points. These points are called "singular points". This property establishes a significant distinction of the collision set of the spatial problem and that of the planar one, where the singular set typically forms a curve (Beauge 1994; Morbidelli et al. 1995; Thomas 1998; Liu & Guzzo 2025) in the space of resonant variables (S, σ).

In Appendix G, we provide graphical representations of the projection of the singular set on the three-dimensional spaces S, A, σ and S, A, α, for $N = -0.85 > N_c$ (left column), showing the intricate changes in the points of the singular set, as the values of certain variables change (see Appendix G and Fig. G.1 for details).

2.2. The perturbing function and the singular set

The perturbing function, $\varepsilon \widehat{H}_1$, is not a perturbation of $\widehat{H}_0$ in a neighborhood of the collision set defined by small values of the function:

$$\|P - P_1\| (S, A, N, \sigma, \alpha, \nu + \theta). \tag{22}$$

Moreover, the Fourier representation of $\widehat{H}_1$ is singular for all points $(S, A, N, \alpha, \sigma)$ in the singular set, and correspondingly any truncated Fourier series,

$$\langle \widehat{H}_1 \rangle := c_0 + \sum_{k=1}^{K} c_k \cos(k(\nu + \theta)) + \sum_{k=1}^{K} s_k \sin(k(\nu + \theta)), \tag{23}$$

with a large truncation order, K, fails to represent the perturbing function in a neighborhood of the singular set defined by small values of

$$\begin{aligned} \mathrm{MRD}(S, A, N, \sigma, \alpha) \\ = \min_{\nu+\theta \in [0,2\pi]} \|P - P_1\| (S, A, N, \sigma, \alpha, \nu + \theta), \end{aligned} \tag{24}$$

which we call the minimum resonant distance (MRD) for a point $(S, A, N, \sigma, \alpha)$ (with evidence, $\mathrm{MRD}(S, A, N, \sigma, \alpha) = 0$ if $(S, A, N, \sigma, \alpha) \in \mathcal{S}$). Note that the MRD may be positive for some values of its argument also when the orbit of P intersects the orbit of P_1, i.e., when the minimum orbital intersection distance (MOID) is equal to zero.

Although in the plane of the resonant variables (σ, S) for fixed values of N, A, α we typically have only a few isolated singular points, their neighborhoods defined by small values of the MRD can extend in the phase-portrait significantly beyond these isolated points. Let us discuss this property with reference to a specific case, depicted in Fig. 2, where on the top panels we represent the level curves of the averaged Hamiltonian on the plane (S, σ) for a fixed value of N, A, α (the pictures were obtained for $N = -0.85, A = -0.05, \alpha = 1.3319$), and on the background for each value of S, σ we represent with a color scale the value of the MRD in units of

$$r_N = \mu_N^{\frac{1}{3}}, \tag{25}$$

where μ_N denotes the reduced mass of Neptune.

The left panel is centered at the resonance, while in the right panel we consider a larger interval of S to localize also the singular point at $S \sim 0.1465$ and $\sigma \sim -0.089$ (indicated with a white box in the top right panel). We observe that from the singular point there emanates a V-shaped set of points characterized by small values of the MRD: a very small MRD for the left branch (between $1.4\, r_N$ and $1.7\, r_N$ inside the resonance region) and a moderately small MRD for the right branch (between $4.5\, r_N$ and $5\, r_N$ inside the resonance region). The region of smaller MRD values is also characterized by folds in the level curves of the averaged Hamiltonian. In this regard, we recall that folds in the phase-portraits of the resonant variables have also been represented in different MMRs (see, for example, Nesvorny et al. 2002; Pan & Gallardo 2025).

To test the correctness of the truncated Fourier representation (23), we compared the values of $\widehat{H}_1$ (and its partial derivatives) with the values of the truncated Fourier series $\langle \widehat{H}_1 \rangle$ (and its partial derivatives, respectively) defined in Eq. (23). In the bottom panels of Fig. 2 we report the results obtained for N, A, α fixed to the values considered for the top panels, while S and σ are in a regularly spaced grid of 500×500 values in the intervals $\sigma \in [0, 2\pi]$ and $S \in [0.19, 0.22]$. For each value of σ, S in the grid, we computed an indicator of the efficiency of the truncated Fourier representation of $\widehat{H}_1$ and its partial derivatives defined by

$$\begin{aligned} \mathcal{E} := \max_{\nu+\theta \in [0,2\pi]} \Big| \mathcal{U}(S, A, N, \sigma, \alpha, \nu + \theta) \\ - \langle \mathcal{U} \rangle (S, A, N, \sigma, \alpha, \nu + \theta) \Big|, \end{aligned} \tag{26}$$

where $\mathcal{U}$ is the disturbing function, $\widehat{H}_1$, or its partial derivatives and $\langle \mathcal{U} \rangle$ its truncated Fourier representation.

In the bottom left panel of Fig. 2, we represent with a color scale the value of $\mathcal{E}$ defined for $\mathcal{U} = \widehat{H}_1$: we clearly appreciate a very small error, $\mathcal{E}$, of the Fourier representation except for the set of points in the left branch with a very small MRD. On the points of the right branch with a moderately small MRD, the Fourier representation of the perturbing function is accurate, though with a larger error of $\mathcal{E} \sim 10^{-5}$ when considering the partial derivative $\mathcal{U} = \frac{\partial \widehat{H}_1}{\partial S}$ (bottom right panel). In fact, the partial derivatives are more singular than the perturbing function itself. We do not report the indicator computed for the partial derivatives with respect to the other variables, since the panels would be very similar to the bottom right one.

These results suggest that the truncated Fourier representation can be used to construct the averaging transformation, except for a neighborhood of the set characterized by very small MRD values (such as the left branch in Fig. 2), identifying deep close encounters of P with P_1. Conversely, for moderately small values of the MRD (such as those represented in the right branch in Fig. 2), which identify weaker close encounters, the Fourier transform can still be used; however, the effectiveness of the averaging method needs to be tested in this case, as the values of the perturbing function and its derivatives are higher.

3. Examples of resonant Lidov–Kozai dynamics and close encounters

In this section we provide examples of orbits in the 1:2 MMR with Neptune for values of N ranging from $N = -1.24$, i.e., below the critical value $N_c \sim -1.08$, to $N = -0.85$ above the critical value. The aim is to show the increment of the complexity of the orbits when close encounters become possible. In particular, we describe the dynamics of orbits that are extracted from the resonance, and that due to the accumulation of the effects of a sequence of weak close encounters migrate toward the nearby MMR. Our explorations consider inclined orbits, from low inclinations of a few degrees up to larger inclinations of about 30 degrees.

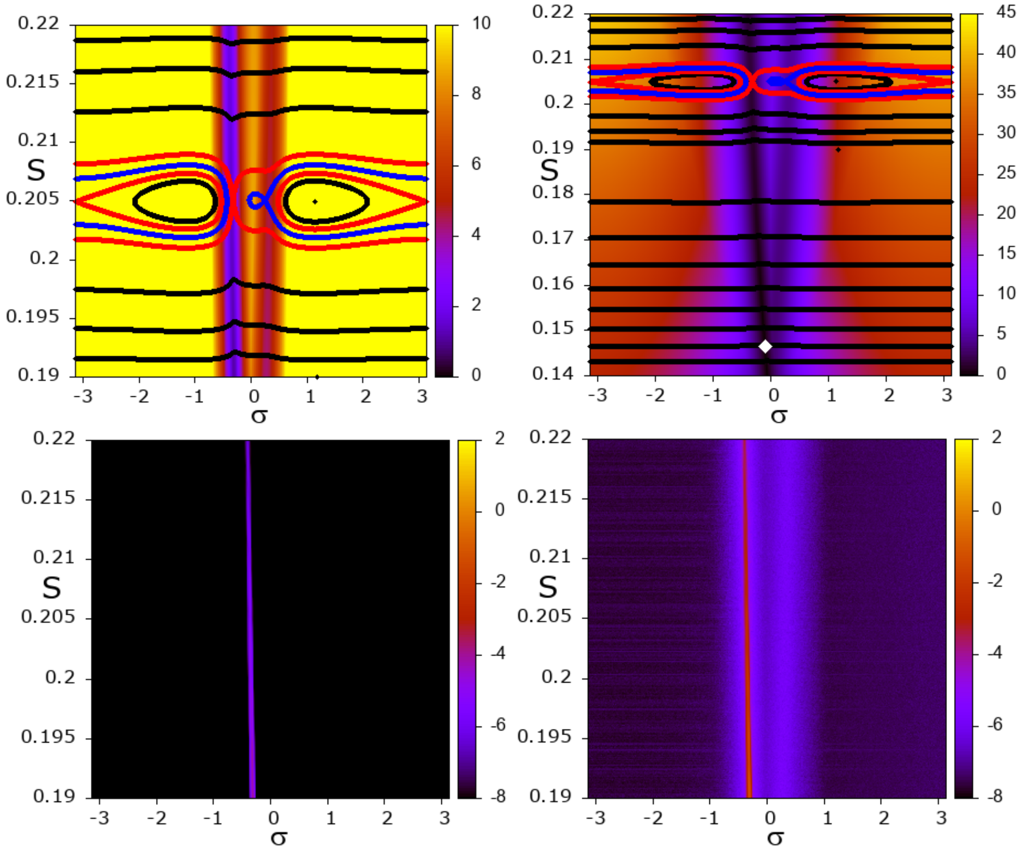

Fig. 2. Top panels: level curves of the averaged Hamiltonian represented on the S, σ plane for the Sun–Neptune case mass ratio, and computed for $N = -0.85, A = -0.05, \alpha = 1.3319$. The level curves were obtained by numerically computing the integral (C.1) on a two-dimensional grid of values, and using the library PGPLOT. The ratio between the MRD and r_N (defined in Eq. (25)) is also represented on the background of the panels using two different color scales. The white square in the top right panel indicates a singular point. Bottom panels: verification of the correctness of the Fourier representation (23) of the disturbing function for $K = 2^9$. The panels represent with a color scale the value of $\log_{10} \mathcal{E}$ computed with $\mathcal{U} = \widehat{H}_1$ (bottom left panel) and $\mathcal{U} = \frac{\partial \widehat{H}_1}{\partial S}$ (bottom right panel) for N, A, α as in the top panels, and σ, S in a two dimensional grid of values. For each value of σ, S in the grid, the coefficients c_k, s_k in Eq. (23) were obtained from a fast Fourier transform of the values of $\widehat{H}_1$ computed on a regular grid of values of $\nu + \theta$, and afterward their derivatives with respect to an action variable were obtained numerically using a difference method.

3.1. Below the critical value

We considered the value of $N = -1.24$ (which is well below the critical value, $N_c \sim -1.08$) for which no close encounters of P with P_1 are possible (this value was chosen for reference with previous studies of the planar case, see Liu & Guzzo (2025) for the Sun–Neptune case and Beauge (1994); Liu & Guzzo (2025) for the Sun-Jupiter case). For this value of N, the resonance is separated from nearby resonances by a region of regular motions at $e = 0$ (planar case). This remains true for low inclinations, as in the case of Fig. 3 (for $N = -1.24$, $S \sim 0.01$, and $A = -0.003$, we have $a \sim 1.587$, $e \sim 0.1$, and $i \sim 4$ deg): the top left panel represents the level curves of the averaged Hamiltonian as well as the MRD, which is larger than $10\, r_N$ (we recall that r_N is defined in Eq. (25)) for all the points of the panel; in the top right panel, we represent with a color scale the values of the Fast Lyapunov Indicator computed for initial conditions with N, A, α as in the top left panel, σ, S in a two-dimensional grid of values, and $\nu, \theta = 0$ (the Fast Lyapunov Indicator was defined and computed here using the non-averaged equations of motion of the spatial CRTBP written using the Kustaanheimo–Stiefel regularization at P_1, see Appendix E for details). The distribution of the values of the FLI is in agreement with the computation of the phase-portrait of the averaged Hamiltonian: the separatrices are replaced by a set, identified by the largest values of the FLI, which in the complete equations of motion of the CR3BP identify chaotic motions, possibly crossing the separatrices of the averaged Hamiltonian. These chaotic motions are embedded in a region of regular motions, identified by the orange color in the picture, providing the indication that the resonance is separated from the nearby MMRs. Therefore, the averaging method is effective and the averaged Hamiltonian accurately represents the resonant dynamics. The time evolution of a sample chaotic orbit with initial conditions σ, S indicated by the black square in the top right panel is also represented ($N, A, \alpha, \nu, \theta$ were chosen as indicated above). The projection of the orbit on the σ, S plane (after the canonical transformation) is represented in the top right panel with a green curve: the orbit projects to a neighborhood of the separatrix separating regions I, II, and III of the phase-portrait, indicating a chaotic evolution. The long-term evolution of the secular variables A, α (after the averaging transformation) is represented in the center panels of Fig. 3, and is well described by the resonant Lidov–Kozai dynamics that is obtained as an application of the theory of adiabatic invariants (Wisdom 1983; Neishtadt 1987a,b; Neishtadt & Sidorenko 2004). According to this theory (whose main aspects are summarized in Appendix D), the time evolution of the variables (α, A) closely follows the level curves of the adiabatic invariant $\mathcal{I}$ (see Eq. (D.2)) on the plane of variables (α, A), defined for a circulation of librational region, until they approach or cross a value

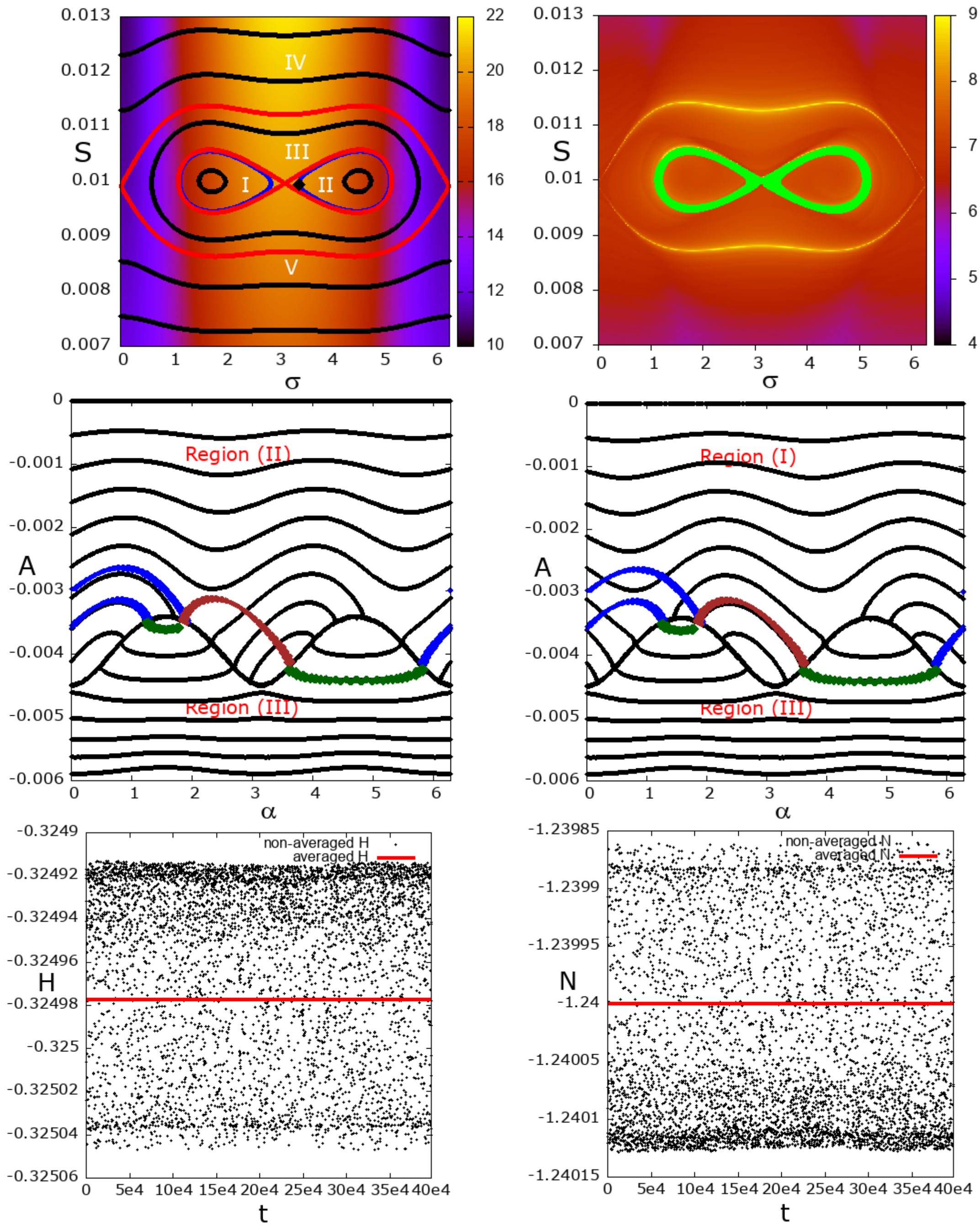

Fig. 3. Adiabatic dynamics for $N = -1.24$, $A = -0.003$, and $\alpha = 0$. Top left panel: level curves of the averaged Hamiltonian in the (σ, S) plane (the separatrices are represented in red) and classification of five different regions of libration and circulation labeled from I to V. The ratio between the MRD and r_N (defined in Eq. (25)) is represented on the background of the panel using a color scale. The black square in region II indicates the initial conditions for an orbit represented in the other panels. Top right panel: regularized FLI in the (σ, S) plane (defined in Appendix E; initial conditions for N, A, α as above, $\nu, \theta = 0$; FLI computed up to $T = 4000$ units of the regularized fictitious time, see Eq. (E.3)) represented with a color scale. The projection of the orbit (after the averaging transformation) with initial conditions for σ, S indicated by the black square in the left panel (computed up to $T = 153\,096$) is represented in green. Center panels: projection of the same orbit (after the averaging transformation) on the plane (α, A) using different colors to indicate the orbit's belonging to region I (red), II (blue), and III (green). The level curves of the adiabatic invariant defined in Eq. (D.2) by fixing the value of the averaged Hamiltonian (to the value corresponding to the fixed initial condition), for the different regions I,II,III are also represented. The bold black curve is due to the different definition of $\mathcal{I}$ at the two sides of the separatrices. The time range represented is $t \in [0, 397\,712]$. At $t = 0$ the orbit is in region II at $A = -0.003$, $\alpha = 0$, and follows a level curve of $\mathcal{I}$ corresponding to region II (blue) represented in the left panel, until it crosses the separatrix to enter region I, and following the corresponding level curve of $\mathcal{I}$ represented in the right panel (red curve). Afterward there is another crossing of the separatrix to enter region III (green), where it follows the corresponding level curve of $\mathcal{I}$ represented in both panels, and finally it returns to region II (blue curve, close to level curves of the left panel). Bottom left panel: conservation of the averaged Hamiltonian before (in black) and after (red) the application of the averaging transformation. Bottom right panel: conservation of the action, N, before (in black) and after (red) the application of the averaging transformation.

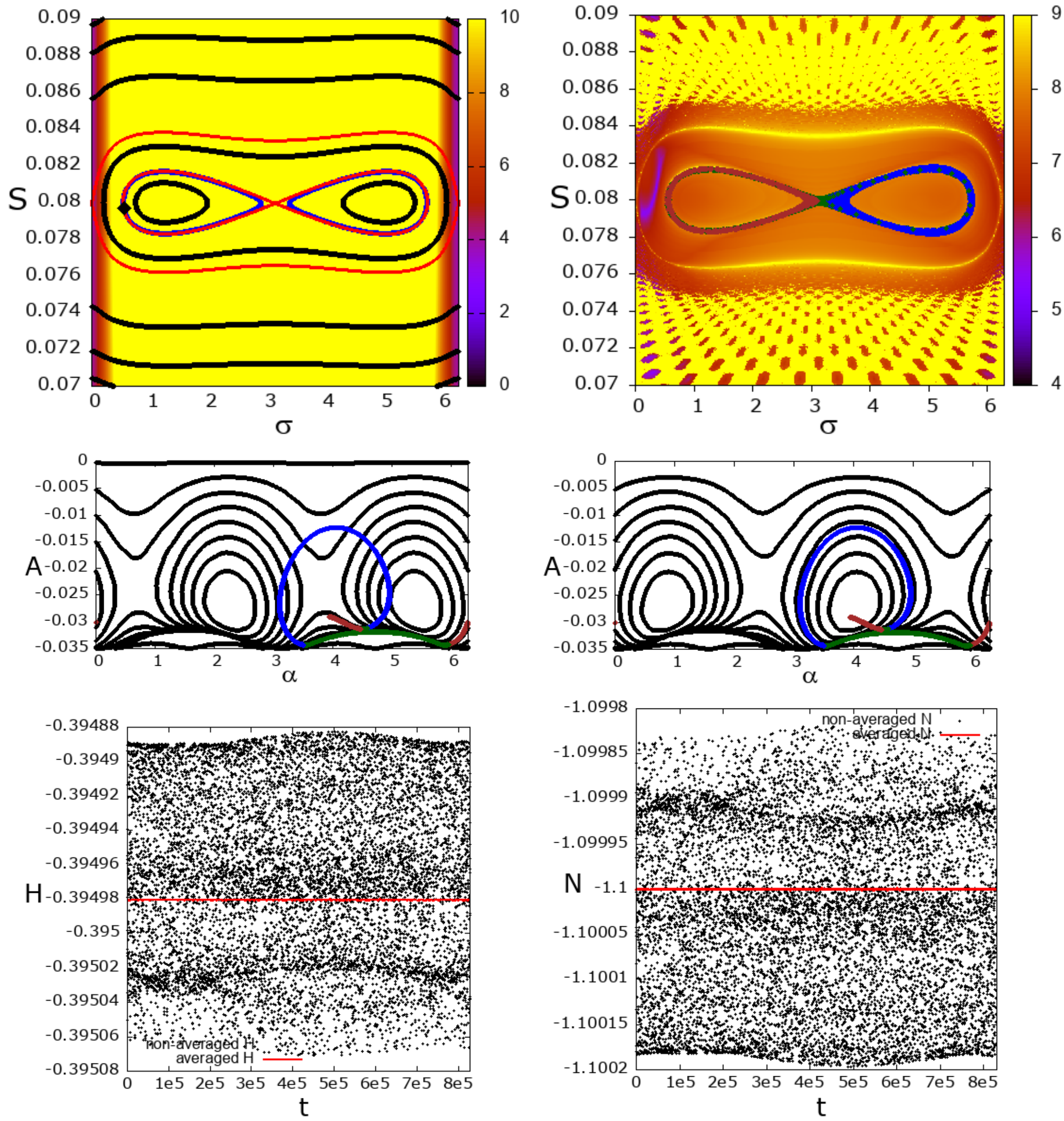

Fig. 4. Adiabatic dynamics for $N = -1.10$, $A = -0.03$, and $\alpha = 0$. Top left panel: level curves of the averaged Hamiltonian in the (σ, S) plane and classification of the regions of libration and circulation from I to V. The ratio between the MRD and r_N (defined in Eq. (25)) is represented on the background of the panel using a color scale (the yellow color means MRD $\geq 9\, r_N$). The black square in region I indicates the initial conditions for an orbit represented in the other panels. Top right panel: regularized FLI in the (σ, S) plane (initial conditions for N, A, α as above, $\nu, \theta = 0$; FLI computed for $T = 4000$, see Eq. (E.3)) represented with a color scale. The projection of the orbit (after the averaging transformation) with initial conditions for σ, S indicated by the black square in the left panel (computed up to $t = 828\,460$) is represented in green, blue, and red (colors explained below). Center panels: projection of the same orbit on the plane (α, A) using different colors to indicate the orbit's belonging to region I (red), II (blue) and (III) green. The level curves of the adiabatic invariant defined in Eq. (D.2) by fixing the value of the averaged Hamiltonian for the different regions I and III (left panel) and the regions II and III (right panel) are also represented. The bold black curve is due to the different definitions of $\mathcal{I}$ at the two sides of the separatrices. The time range represented is $t \in [0, 828\,460]$. At $t = 0$ the orbit is in region I at $A = -0.03$, $\alpha = 2\pi$, and follows a level curve of $\mathcal{I}$ corresponding to region I (red) represented in the left panel, until it crosses the separatrix to enter region (III), and following the corresponding level curve of $\mathcal{I}$ represented in green. Afterward there is another crossing of the separatrix to enter region II (blue, see the right panel), and finally it returns to region I (red, see the left panel). Bottom left panel: conservation of the averaged Hamiltonian before (in black) and after (red) the application of the averaging transformation. Bottom right panel: conservation of the action, N, before (in black) and after (red) the application of the averaging transformation.

corresponding to the boundary of the region. In the center panels we use different colors to indicate the orbit's belonging to region I (red), II (blue), and (III) green. The level curves of the adiabatic invariant defined in Eq. (D.2) by fixing the value of the averaged Hamiltonian (to the value corresponding to the fixed initial condition), for the different regions, I, II, and III, are also represented. The bold black curve is due to the different definition of $\mathcal{I}$ at the two sides of the separatrices. At $t = 0$ the orbit is in region II at $A = -0.003$, $\alpha = 0$, and follows a level curve of $\mathcal{I}$ corresponding to region II (blue) represented in the left panel, until it crosses the separatrix to enter region (I), and following the corresponding level curve of $\mathcal{I}$ represented in the right panel (red curve). Afterward there is another crossing of the separatrix to enter region III (green) where it follows the corresponding level curve of $\mathcal{I}$ represented in both panels, and finally it returns to region II (blue curve, close to the level curves of the left panel). The multiple crossing of a separatrix is identified in the literature as a source of chaos (adiabatic chaos or

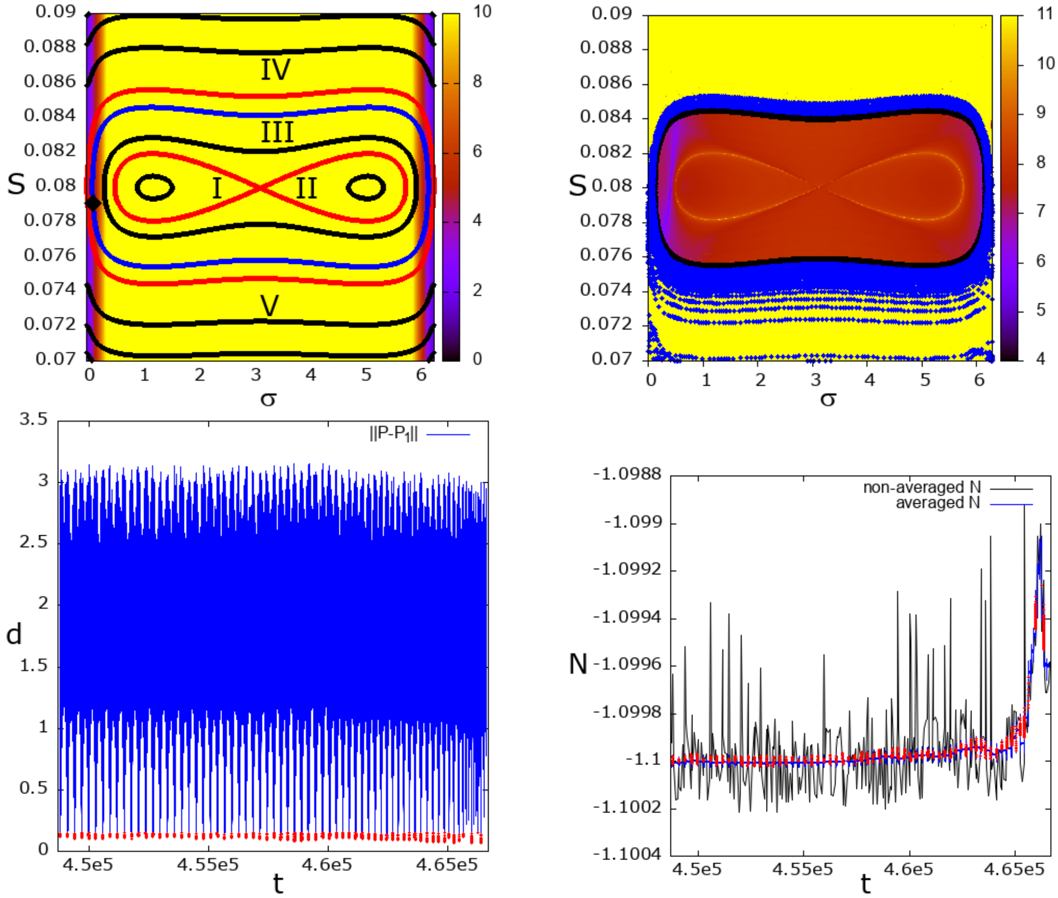

Fig. 5. Adiabatic dynamics for $N = -1.10$, $A = -0.01$, and $\alpha = 0$. Top left panel: level curves of the averaged Hamiltonian in the (σ, S) plane and classification of the regions of libration and circulation from I to V. The ratio between the MRD and r_N (defined in Eq. (25)) is represented using a color scale. The black square in region III indicates the initial conditions for an orbit represented in the other panels. Top right panel: regularized FLI in the (σ, S) plane represented with a color scale (initial conditions for N, A, α as above, $\nu, \theta = 0$; FLI computed for $T = 4000$, see Eq. (E.3)). The projection of the orbit (after the averaging transformation) with initial conditions for σ, S indicated by the black square in the left panel is also represented (in black for $t \leq 448\,766$ and in blue for $t \in (448\,766, 466\,610]$). In the bottom left panel, we represent the variation in the distance, $\|P - P_1\|$, for $t \in (448\,766, 466\,610]$; the red dots sample points of the graph for which P has a close encounter with P_1 at a distance smaller than 0.15. In the bottom right panel, we represent the time variation in the action, N, before (in black) and after (in blue) the averaging transformation (red dots as in the bottom left panel). The time evolution of the orbital elements a, e is represented in Fig. G.2.

geometric chaos, depending on the context). The bottom panels show the very good conservation of the averaged Hamiltonian and of the action, N, for the same orbit, confirming the efficacy of the averaging method.

3.2. Near the critical value

We considered the value of $N = -1.10$, which, although below the critical value $N_c \sim -1.08$, is sufficiently close to it to make close encounters between P and P_1 possible. We highlight two different kinds of chaotic motion.

The first one, represented in Fig. 4, is very similar to the example shown in Section 3.1, with chaotic dynamics produced by the crossing of separatrices and without close encounters playing any significant role (the MRD is larger than $10\, r_N$ along the orbit, see Fig. 4, top left panel). A choice of an initial condition close to the separatrix between regions I, II, and III produces a chaotic orbit crossing several times the separatrix, and the secular evolution is well described by the adiabatic approximation (center panels of Fig. 4). The time evolution of the averaged Hamiltonian and of the action, N (computed after the averaging transformation), shows very small variations (bottom panels), with a very good efficacy of the averaging transformation in the reduction of the oscillations with respect to the mean value of these quantities.

In the second example, represented in Fig. 5, close encounters play a crucial role in shaping the chaotic dynamics: the initial condition (the black square in the top left panel) is in the libration region III very close to the larger separatrix. Thus, at each libration, the orbit crosses a region of MRD close to $2\, r_N$ where P may have close encounters with P_1 and may also experience transitions from region III to region IV and vice versa. The FLI color map (top right panel) shows that region IV is characterized by a large FLI value, indicating chaotic motions. The projection of the orbit on the FLI color map is represented in black for $t \leq 448\,766$ and in blue for $t \in (448\,766, 466\,610]$. In the former time interval the orbit is in region III, while in the latter one the orbit performs a transition to region IV. In the bottom left panel, we represent the variation in the distance $\|P - P_1\|$ for $t \in (448\,766, 466\,610]$. The red dots sample points of the graph for which P has a close encounter with P_1 at a distance smaller than 0.15; the close encounters are with evidence clustered, due to the slow variation in the resonant variables. Up to this point, the description is similar to that

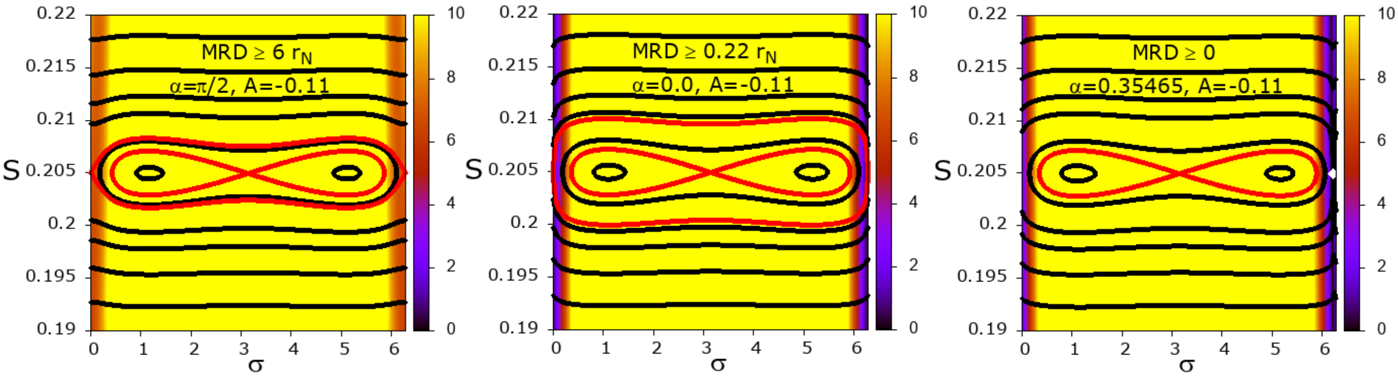

Fig. 6. Level curves of the averaged Hamiltonian on the σ, S plane for the Sun–Neptune mass ratio, $N = -0.85, A = -0.11$, and $\alpha_* = \pi/2$ (left), $\alpha = 0$ (center), $\alpha = \alpha_* = 0.35465...$ (right). The ratio between the MRD and r_N is represented on the background of the panels using a color scale; the minimum value attained on the panel is also indicated. The red level curves contain critical points of the averaged Hamiltonian; the white square in the right panel indicates a singular point.

given for the orbits represented in Figs. 3 and 4. However, a significant difference emerges from the graphs representing the time variations in the averaged Hamiltonian, $\widehat{H}$, and in the actions, N. In the bottom right panel, we represent the variation in the action, N, before (in black) and after (in blue) the averaging transformation for $t \in [448\,766, 466\,610]$: we see that while the averaging transformation is effective in reducing the local oscillations of N (compare the amplitude of the local oscillations of the black curves to the local oscillations of the blue curves), the blue curves show larger variations that are correlated with the close encounters identified by the minima of $\|P - P_1\|$ (represented in the left panel). A similar behavior is observed for the time variation in $\widehat{H}$ (not represented for brevity), while for the orbital elements a, e, whose time evolution is less stable than the time evolution of N and $\widehat{H}$, the averaging transformation is still effective in reducing the local oscillations (see Fig. G.2). In the time interval between each pair of close-encounter clusters, the averaged values of $\widehat{H}$ and N are almost constant, but before and after each close-encounter cluster they have a jump, which can accumulate in an apparently random way. These small, random, almost-stepwise variations in N and of $\widehat{H}$ were also detected for the planar problem (see Liu & Guzzo 2025) and are similar to the Arnold diffusion detected in Guzzo et al. (2020) for a generic quasi-integrable system. In the spatial problem, the variations in N and $\widehat{H}$ produce an additional source of chaos and diffusion with respect to the mechanism of adiabatic chaos found for the orbits of Figs. 3 and 4. For example, for an orbit that remains in the same circulation region, the variation in N and $\widehat{H}$ may determine a drift of the orbit far from the 1:2 MMR.

3.3. Above the critical value

We considered the value of $N = -0.85$, for which the singular set is not empty, and correspondingly we may have orbits of P that cross the orbit of P_1. The appearance of singular points in the resonant planes (σ, S) for given values of A, α was discussed in Section 2.1: we refer to Fig. G.1 for a detailed discussion and, in particular, for $N = -0.85$ the points in the singular set satisfy $-0.117... < A < 0$. We here provide more details about the properties of the level sets of the averaged Hamiltonian in the (σ, S) planes, which are determined by the appearance and the position of the singular points with respect to the resonance. In Fig. 6 we provide three examples for $A = -0.11$, close to its lower value for the appearance of the singular points. In this case, there are singular points in the (σ, S) plane only for specific values of α, and three model cases are represented in the panels of the figure. For $\alpha = \pi/2$ (left panel) there are no singular points, and the *MRD* on the panel is larger than $6.4\, r_N$. For $\alpha = 0$ (center panel) there are singular points, but they are located outside the resonant region identified by the separatrices represented in red. For $\alpha = 0.35465...$ (right panel) there is a singular point inside the resonant region. Since in a small neighborhood of the singular point the averaged Hamiltonian is not conjugate to the original Hamiltonian by the averaging transformation defined in Appendix B, we do not represent the level curves of $\widehat{H}$ passing through a small neighborhood of the singular point, and so in this case we lose the larger separatrix that is represented in the left and center panels. The lack of a separatrix curve does not prevent the definition of different regions of the σ, S points, according to the libration or circulation properties of the angle, σ, along a level curve of $\widehat{H}$.

In Fig. 7, we provide three examples for $A = -0.02$, close to its upper value. In this case, there are singular points in the (σ, S) plane for all the values of α (see Fig. G.1), so we have different possibilities depending on whether the singular point is in the resonant region or not. For $\alpha = 0.5$ (left panel) the singular points are outside the resonant region. Nevertheless, we have relatively small values of the MRD$\geq 3\, r_N$; we also note that this phase portrait exhibits greater complexity, characterized by three separatrices, compared to the cases depicted in Fig. 6. For the values of α as in the center and right panels we have a singular point within the resonant region (indicated with a while square), and correspondingly we lose a saddle point with its level set.

In the following, we present examples of two different kinds of motions, selected according to the different impact of close encounters on their long-term dynamics. The first one refers to motions that are well within the resonant domain in the σ, S plane, so that they do not have deep close encounters with P_1; for example, they may be close to or inside the innermost separatrices in the panels of Fig. 6, or correspond to values of A for which there are not deep close encounters. Since in these cases we expect very good conservation of $\widehat{H}$ and N (after averaging) along the motion, we analyzed orbits with the same initial value, h, of the averaged Hamiltonian (in addition to N) so that we could compare their projection on the α, A secular plane with the level curves of the adiabatic invariants obtained by fixing both values of $\widehat{H}$ and N. Fig. 8 shows the dynamics of two chaotic orbits with initial value h identifying the innermost separatrix of the

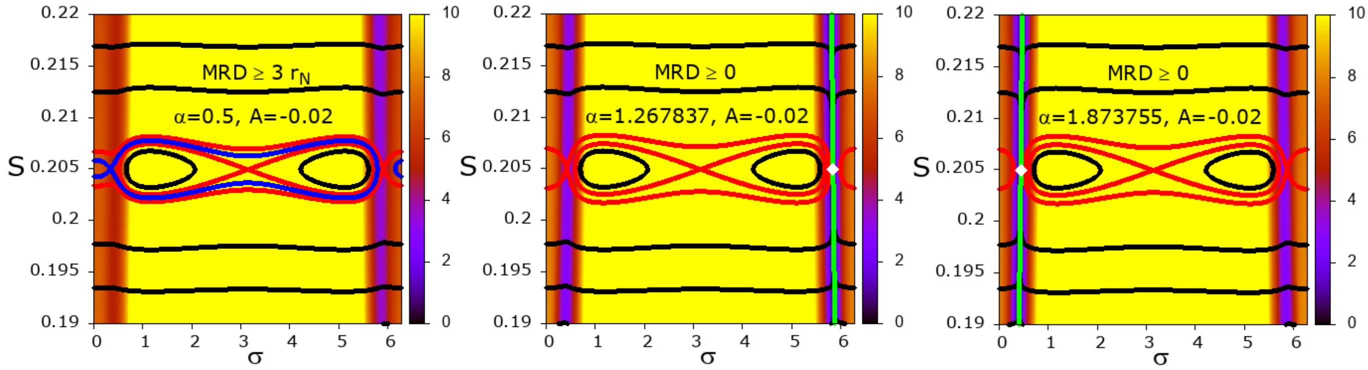

Fig. 7. Level curves of the averaged Hamiltonian represented on the σ, S plane for the Sun–Neptune mass ratio, $N = -0.85, A = -0.02$, and $\alpha = 0.5$ (left), $\alpha = 1.267837$ (center), $\alpha = 1.873755$ (right). The ratio between the MRD and r_N is represented on the background of the panels using a color scale; the minimum value attained on the panel is also indicated. The red level curves contain critical points of the averaged Hamiltonian; the white square in the right panel indicates a singular point; the light blue lines represent the curve $\sigma = \hat{\sigma}(S, A, N)$ (see Eq. (20)).

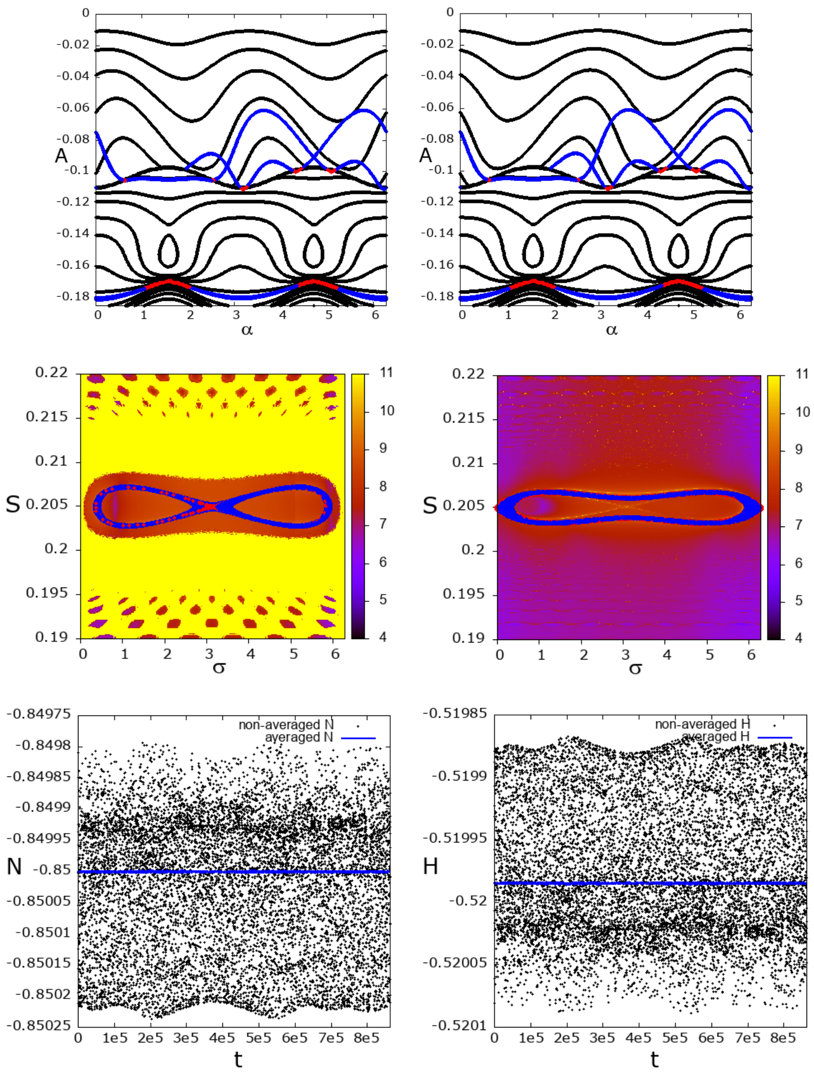

Fig. 8. Dynamics of two orbits selected for $N = -0.85$, $h = -0.51998502949854775$, and $A = -0.11, \alpha = 0$ (orbit 1); $A = -0.18, \alpha = 0$ (orbit 2). Top panels: projection of the two orbits on the (α, A) plane (after averaging), for $t < 863\,000$ (orbit 1, on the top) and $t < 744\,500$ (orbit 2, on the bottom). The red dots indicate when the orbits are very close to a separatrix. In the same panel, we also represent the level curves of the adiabatic invariant, $\mathcal{I}$, (see Eq. (D.2)) for the given value, h, of the averaged Hamiltonian and of N, and for the regions I, III, and IV (from top to bottom in the left panel) and for the regions II, III, and IV (from top to bottom in the right panel). The bold curves represent the separatrices between different zones. Center panels: projection of orbit 1 (left panel) and orbit 2 (right panel) on the (σ, S) plane (after averaging). In the background we represent the FLI computed of the initial values of α, A of orbit 1 and 2, respectively, for $T = 10\,000$ (see Eq. (E.3)). In the bottom panels, we represent the time evolution of the action, N (left), and of the averaged Hamiltonian, $\widehat{H}$ (right), before (in black) and after (red) the application of the averaging transformation, for orbit 1.

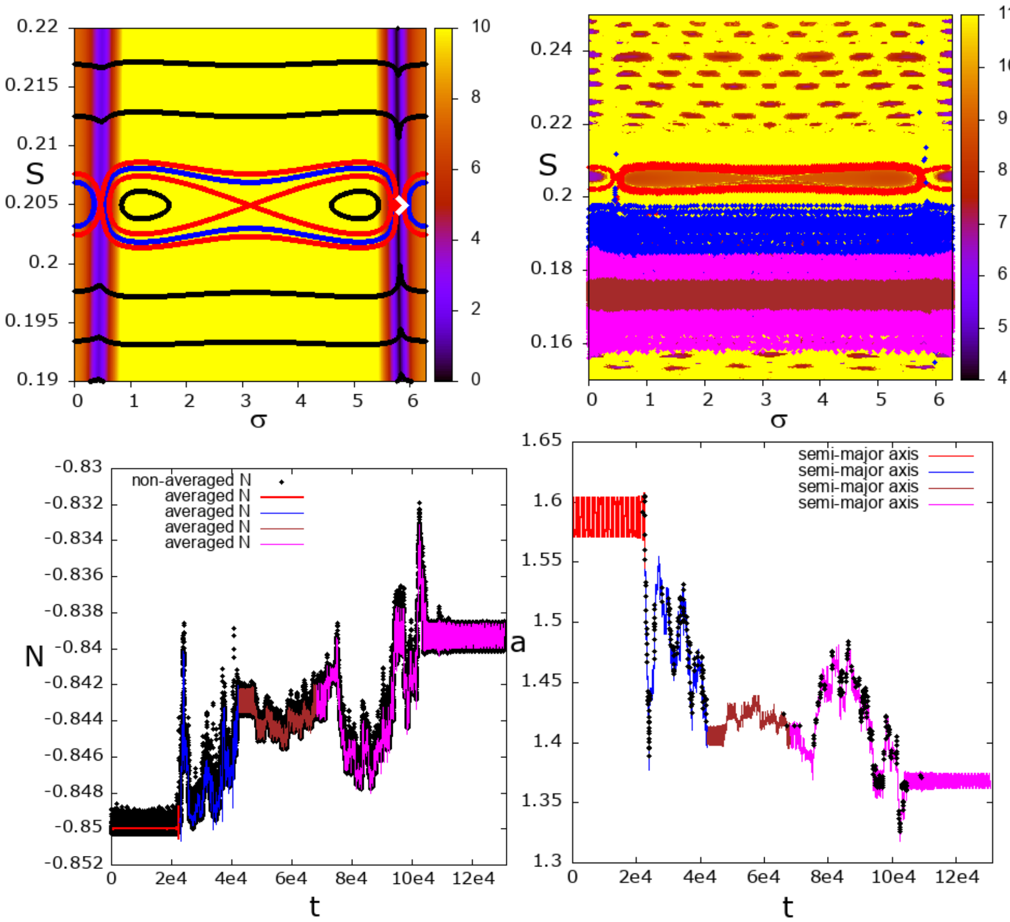

Fig. 9. Top left panel: level curves of the averaged Hamiltonian represented on the σ, S plane for $N = -0.85, A = -0.01$, and $\alpha = 1.316903$. The ratio between the MRD and r_N is represented in the background of the panels using a color scale. The white square indicates a singular point. The red square (very close to the singular point) indicates the initial values of σ, S for the orbit analyzed in the other panels. Top right panel: projection on the (σ, S) plane (after averaging) of the orbit with initial conditions indicated in the right panel, for $t < 130\,855$. In the background we represent the FLI computed for the same initial values of α, A and $T = 10\,000$ (see Eq. (E.3)). The different colors used for the orbit projection correspond to different time intervals (red, blue, brown, and magenta for [0, 22 603], [22 603, 42 281.2], [42 281.2, 68 246], and [68 246, 130 854.7], respectively). Bottom left panel: time evolution of the action, N, before (black) and after (red, blue, brown, and magenta as explained above) the application of the averaging transformation. Bottom right panel: time evolution of the value of the semimajor axis. The black dots indicate a close encounter at distance $\|P - P_1\| < 0.05$. The time evolution of the orbital elements a, e are represented in Fig. G.3.

center panel in Fig. 6. The projection of the orbits on the planes α, A is represented in the top panels: orbits 1 and 2 are chaotic, and their secular dynamics follow the level curves of the adiabatic invariants defined for the regions I,III, II,III, and III,IV, respectively (the classification of the regions I,..,V was done as in the top left panel of Fig. 4). The good agreement of the secular dynamics of all these orbits with the level curves of the adiabatic invariants represented in the top panel is a consequence of the very good conservation of N and $\widehat{H}$ along the orbits (the time variation in N and $\widehat{H}$ for orbit 1 is represented in the bottom panels; the time variations for orbit 2, not represented for brevity, have very similar behavior). We also remark that these orbits, despite corresponding to the large value of $N = -0.85$, are not subject to deep close encounters: along the numerical integration we detected that the minimum value of $\|P - P_1\|$ is larger than $8\, r_N$ for both orbits. In the center panels we represent the projection of the two orbits on the σ, S plane (after averaging), with the value of the FLI reported in the background: we notice that both chaotic orbits are surrounded by regions of regular motion.

The second kind of resonant dynamics contains motions that initially are in the peripheral region of the resonance and that are characterized by deep close encounters with P_1. In Fig. 9 we consider initial values of N, A, α for which we have a singular point in the resonant region of the σ, S plane (white point in the top right panel), as well as a region characterized by small values of the MRD crossing the resonance. The red point in the panel (very close to the singular point) belongs to the large libration highlighted in blue, and indicates the initial conditions of σ, S for the orbit analyzed in the other panels that represent the project on the σ, S plane (top right panel) and the time evolution of N (bottom left) and of the semimajor axis (bottom right). Different time intervals are highlighted with different colors: in the first time interval (correspondingly, the projection on the σ, S plane is in red; top right panel) the orbit is performing large librations with $\|P - P_1\| \sim 0.06$, but at the end of the interval crosses the larger separatrix and afterward, close encounters at $\|P - P_1\| \sim 0.015$ extract the orbit from the resonance. In Figs. G.3 and G.4, we appreciated that the averaging transformation is still effective in reducing the local oscillations of the semimajor axis, except for during the deepest close encounters. In the next time interval (indicated in blue), the orbit is outside the larger separatrix and performs circulations crossing the

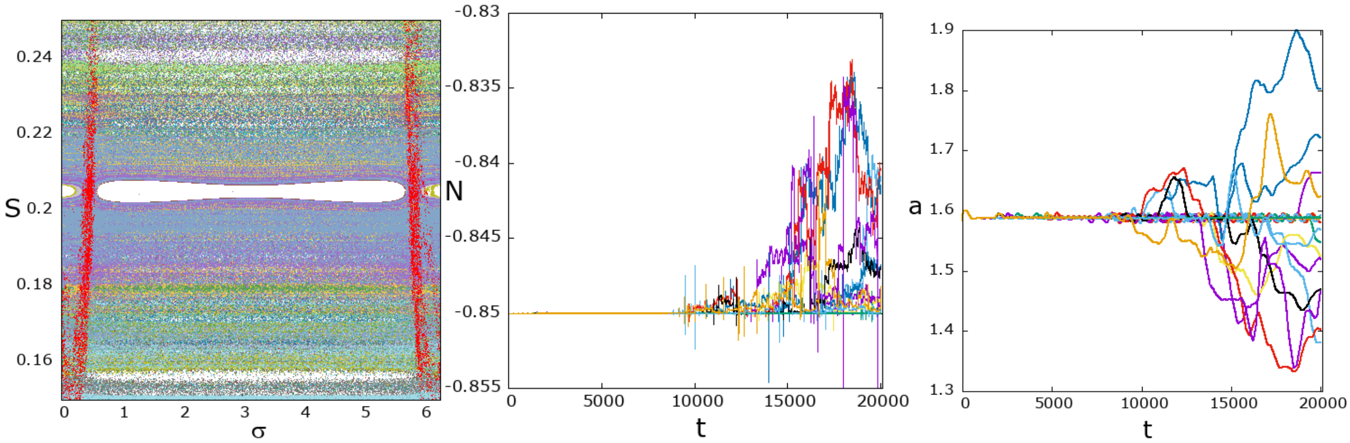

Fig. 10. Diffusion in the phase space for orbits with 20 initial conditions close to the orbit previously selected for Fig. 9. The 20 initial conditions have the same value of N, A, α, while σ, S are regularly spaced in a segment joining $(\sigma_1, S_1) = (5.7229756139649535, 0.20490981963927857)$ and $(\sigma_2, S_2) = (5.7229573588698726, 0.20496993987975951)$. For the 20 orbits we represent: the projection on the (σ, S) plane (after averaging) for a maximum value of t in a range between 10^5 and $2\,10^5$ corresponding to the same fictitious regularized time (left panel; the red dots indicate where a close encounter at $\|P - P_1\| < 0.05$ occurs); the time evolution of N (after averaging; center panel); and the time evolution of the semimajor axis (right panel; a running average along a window of $\Delta t = 500$ has been applied).

region of small MRD determining variations of N (and of the averaged Hamiltonian, not reported for brevity) and also of the semimajor axis. This sequence of close encounters determines the diffusion of the orbit toward a nearby resonance of larger order. In fact, at the beginning of the third time interval (indicated in brown) the semimajor axis oscillates close to $a \sim 1.41$, and after other sequences of close encounters it oscillates close to $a \sim 1.36$ (at the end of the magenta interval). The diffusion toward nearby resonances is also represented in Fig. 10 for a set of 20 orbits with very close initial conditions near the initial conditions for σ, S indicated by the red dot in the top left panel of Fig. 9. In the left panel, we see the diffusion of the set of orbits from the border of the resonance to its exterior, due to a sequence of close encounters (indicated by the red dots). The accumulation of the effects of close encounters determines also the chaotic diffusion of the action, N. The exit from the 1:2 MMR resonance is also appreciated from the spread of the values of the semimajor axis, reported in the right panel.

4. Conclusions

The analysis of the singular sets and the computation of the FLI and MRD allow to select and analyze the behavior of orbits in a MMR of the spatial CRTBP having close encounters with a planet. There is a difference in the chaotic diffusion when close encounters may happen only at moderate distance from the planet: in such a case, we have two quasi-conserved quantities (N and $\widehat{H}$), so the secular dynamics may be analyzed by considering the level curves of the adiabatic invariant, obtained for fixed values of $N, \widehat{H}$, in the plane of the secular variables (α, A). In this case, we observe the well-known mechanism of chaos generation due to the crossing of a separatrix. Instead, when deep close encounters are possible, we also observe a step-wise diffusion of N and $\widehat{H}$, which superimposes on the chaotic effects due to the crossing of a separatrix. For some orbits, this diffusion determines the extraction from the given MMR and its migration toward other MMRs, overlapping with the initial one. The analytic characterization of this diffusion, in our opinion, could be done in a future work by developing for the specific case of the semi-analytic theory of Guzzo et al. (2020).

Acknowledgements. The authors wish to thank Prof. V. Sidorenko for a useful discussion and advice on the use of adiabatic invariants. This work is part of XL's PhD work (supervisor MG, co-supervisor Elena Lega). X.L. also acknowledges the support of the China Scholarship Council. X.L. acknowledges the support by the Fundamental Research Funds for the Central Universities of Prof. L. Zhao.

References

Beauge, C. 1994, Celest. Mech. Dyn. Astron., 60, 225
Chirikov, B. V. 1979, Phys. Rep., 52, 263
Efimov, S. S., & Sidorenko, V. V. 2020, Cosmic Res., 58, 249
Fenucci, M., Gronchi, G. F., & Saillenfest, M. 2022, Celest. Mech. Dyn. Astron., 134, 23
Ferraz-Mello, S. 1987, A&A, 183, 397
Ferraz-Mello, S. 2007, Canonical Perturbation Theories, Degenerate Systems and Resonance (Berlin: Springer)
Ferraz-Mello, S., & Sato, M. 1989, A&A, 225, 541
Gallardo, T. 2020, Celest. Mech. Dyn. Astron., 132, 9
Gronchi, G. F., & Milani, A. 1998, Celes. Mech. Dyn. Astron., 71, 109
Gronchi, G. F., & Tardioli C. 2012, DCDS Ser. B, 18, 1323
Guzzo, M. 2024, Nonlinearity, 37, 105011
Guzzo, M., & Lega, E. 2018, Physica D, 373, 38
Guzzo, M., & Lega., E. 2023, Celest. Mech. Dyn. Astron., 135, 37
Guzzo, M., Efthymiopoulos, C., & Paez, R. 2020, J. Nonlinear Sci. 30, 851
Henrard, J., & Lemaitre, A. 1983, Celest. Mech., 30, 197
Lemaitre, A. 1984, Celest. Mech., 32, 109
Lidov, M. L., & Ziglin, S. L. 1974, Celest. Mech., 9, 151
Liu, X., & Guzzo M. 2025, Celest. Mech. Dyn. Astron., 137, 1
Maró, S., & Gronchi, G. 2018, SIAM J. Appl. Dyn. Syst., 17, 1786
Milani, A., & Baccili, S. 1998, Celest. Mech. Dyn. Astron., 71, 35
Moons, M. 1994, Celest. Mech. Dyn. Astron., 60, 173
Morbidelli, A. 1997, Icarus, 127, 1
Morbidelli, A. 2002, Modern Celestial Mechanics: Aspects of Solar System Dynamics
Morbidelli, A., & Guzzo, M. 1997, Celest. Mech. Dyn. Astron., 65, 107
Morbidelli, A., Thomas, F., & Moons, M. 1995, Icarus, 118, 322
Neishtadt, A. I. 1987a, Dokl. Akad. Nauk SSSR, 295, 47
Neishtadt, A. I. 1987b, Prikl. Mat. Mekh., 51, 750
Neishtadt, A. I., & Sidorenko, V. V. 2004, Celest. Mech. Dyn. Astron. 90, 307
Nesvorny, D., & Roig, F. 2000, Icarus, 148, 282
Nesvorny, D., & Roig, F. 2001, Icarus 150, 104
Nesvornỳ, D., Thomas, F., Ferraz-Mello, S., & Morbidelli, A. 2002, Celest. Mech. Dyn. Astron., 82, 323
Öpik, E. J. 1976, Interplanetary Close Encounters (New York: Elsevier).
Pan, N., & Gallardo, T. 2025, Celest. Mech. Dyn. Astron., 137, 2
Roig, F., Simula, A., Ferraz-Mello, S., & Tsuchida, M. 1998, A&A, 329, 339
Rossi, M., & Guzzo, M. 2024, Physica D, 463, 134173

Saillenfest, M., Fouchard, M., Tommei, G., & Valsecchi, G. B. 2016, Celest. Mech. Dyn. Astron., 126, 369
Schubart, J. 1964, Smithsonian Astrophys. Obs. Spec. Rep., 149
Schubart, J. 1966, Special Cases of the Restricted Problem of Three Bodies, The Theory of Orbits in the Solar System and in Stellar systems, ed. G. Contopoulos , 187
Sidorenko, V. V. 2006, Cosmic Res., 44, 440
Sidorenko, V. V. 2023, Celest. Mech. Dyn. Astron., 136, 25
Sidorenko, V. V., Neishtadt, A. I., & Zelenyi, L. M. 2014, Celest. Mech. Dyn. Astron., 120, 131
Thomas, F. 1998, La dynamique résonnante dans le système solaire: application au mouvement des objects transneptuniens, PhD dissertation, Observatoire De Paris
Valsecchi, G. B. 2002, Close Encounters in Öpik Theory, eds. D. Benest, & C. Froeschlé, Singularities in Gravitational Systems. Lecture Notes in Physics (Springer)
Winter, O., & Murray, C. 1997a, A&A, 319, 290
Winter, O., & Murray, C. 1997b, A&A, 328, 399
Wisdom, J. 1983, Icarus, 56, 51

Appendix A: On the dependence of H on $\nu + \theta$

In this Appendix we show that the Hamiltonian depends on the angles $\sigma, \alpha, \nu, \theta$ defined in Eq. (4) only through $\sigma, \alpha, \nu + \theta$ when $q - p = 1$.

We first consider the dependence of H_1 on the orbital elements $a, e, i, f, \omega, \Omega, \lambda_1$. Using Eq. (1.71) of Morbidelli (2002) we have:

$$H_1 = -\frac{1}{|\mathbf{r} - \mathbf{r}_1|} + \frac{\mathbf{r} \cdot \mathbf{r}_1}{|\mathbf{r}_1|^3} \tag{A.1}$$

$$= -\frac{1}{\sqrt{r^2 + 1 - 2r\cos\psi}} + r\cos\psi \tag{A.2}$$

where $r = \frac{a(1-e^2)}{1+e\cos f}$ and ψ is the angle between P and P_1. Using Eqs. (1.9), (1.10), (1.11) and (1.12) of Morbidelli (2002) we also obtain:

$$\cos(\psi) = \cos(i)\sin(f + \omega)\sin(\lambda_1 - \Omega) + \tag{A.3}$$

$$\cos(f + \omega)\cos(\lambda_1 - \Omega). \tag{A.4}$$

Therefore, since r depends only on the angle f we have that H_1 depends on the angles $f, f + \omega, \lambda_1 - \Omega$. Let us now consider the dependence of H_1 on the modified Delaunay variables $\Lambda, \Phi, \Lambda_1, \lambda, \varphi, \gamma, \lambda_1$ defined in Section 2. Since f depends on $\lambda + \varphi$ (which is the mean anomaly M) and $\lambda_1 - \Omega = \lambda_1 + \gamma$, $\omega = \gamma - \varphi$, and $q = p + 1$, using Eq. (4b) we obtain that H_1 depends on $\sigma, \alpha, \nu, \theta$ through:

$$\lambda + \varphi = \sigma + p(\nu + \theta), \tag{A.5}$$

$$\lambda_1 + \gamma = \sigma - \alpha + q(\nu + \theta), \tag{A.6}$$

$$\gamma - \varphi = -\alpha. \tag{A.7}$$

Appendix B: Definition of the averaging transformation

The averaging transformation ψ is defined and computed using the Lie method as the time-ε Hamiltonian flow of the generating function:

$$\chi = \sum_{k \geq 1} \left[b_k \sin(k(\nu + \theta)) + d_k \cos(k(\nu + \theta)) \right], \tag{B.1}$$

with coefficients $b_k(N, S, A, \sigma, \alpha)$ and $d_k(N, S, A, \sigma, \alpha)$ given by

$$b_k = \frac{c_k}{k\left(\frac{\partial \widehat{H}_0}{\partial N} + \frac{\partial \widehat{H}_0}{\partial \Theta}\right)}, d_k = -\frac{s_k}{k\left(\frac{\partial \widehat{H}_0}{\partial N} + \frac{\partial \widehat{H}_0}{\partial \Theta}\right)}. \tag{B.2}$$

The canonical transformation is effectively computed with the Lie method by numerically computing the Fourier coefficients c_k, s_k of the perturbing function (see Eq. (6)) as well as their derivatives, using the method of Schubart Schubart (1964, 1966) by extending to the spatial case the implementation of Liu & Guzzo (2025). The numerical computation of ψ is necessary in order to compare the time evolution of the non-averaged variables with the time evolution of the averaged ones.

Appendix C: Numerical computation of the averaged Hamiltonian of the Fourier coefficients

For the panels of Fig. 2 both the averaged Hamiltonian and the Fourier expansion (6) have been obtained from numerical computations of the coefficients of the perturbing function using Schubart's method Schubart (1964, 1966). Precisely, the level curves of the averaged Hamiltonian (as the top panels of Fig. 2, the top-left panels of Figs. 3, 4, 5, 9, and all panels of Figs. 6, 7) are obtained by numerically computing the integral:

$$\widehat{H} = \widehat{H}_0 + \frac{\varepsilon}{2\pi} \int_0^{2\pi} \widehat{H}_1 d(\nu + \theta), \tag{C.1}$$

while the coefficients c_k, s_k and their derivatives are computed using a Fast Fourier Transform of the values of $\varepsilon\widehat{H}_1$ and a difference method (we extend to the spatial case the implementation of Liu & Guzzo (2025)).

Appendix D: Adiabatic invariants for the CRTBP

The use of adiabatic invariants to study the long-term dynamics of MMRs of the spatial CRTBP is well established; see, for example, Wisdom (1983); Neishtadt (1987a); Neishtadt & Sidorenko (2004); Sidorenko (2006); Sidorenko et al. (2014); Milani & Baccili (1998); Efimov et al. (2020); Sidorenko (2024); Morbidelli (2002); Nesvorny et al. (2002); Saillenfest et al. (2016); Fenucci et al. (2022). Since the equations of motion of the averaged Hamiltonian have different timescales, the shorter one characterizing the time evolution of the resonant variables S, σ and the longer one characterizing the time evolution of A, α, it is natural to apply the theory presented in Neishtadt (1987b) for Hamiltonian systems of 2 dof with fast and slow evolution. In this Section, we recall the fundamental aspects of this theory that are utilized also in this paper, to study the dynamics of the 1:2 MMR.

(i) Within the timescale $T << \frac{1}{\varepsilon}$ the slower variables (α, A) could be regarded as frozen to a constant value, and the motion of the faster variables (σ, S) could be described by the corresponding "frozen" Hamiltonian (see Eq. (10)):

$$\widehat{h}(S, \sigma; N_0, A_0, \alpha_0) := -\frac{1}{(qS - N_0)^2} - n_1 pS + \varepsilon c_0(S, A_0, N_0, \sigma, \alpha_0), \tag{D.1}$$

where (N_0, A_0, α_0), which are the initial values of the corresponding action-angle variables, are treated as parameters. In suitable librational or rotational domains of the one-degree of freedom reduced Hamiltonian $\hat{h}$ one introduces the action-angle variables $\phi, \mathcal{I}$, where

$$\mathcal{I} = \frac{1}{2\pi} \oint_{\hat{h}=h} S\, d\sigma, \tag{D.2}$$

is called adiabatic invariant (the integration is defined on the cycle $\hat{h} = h$ corresponding to a libration or a circulation), and ϕ is a conjugate angle. The integral is related to an area enclosed or delimited by the integration path.

(ii) To account for the time variation of the secular variables A, α, in accordance with the theory presented in Neishtadt (1987b), a canonical transformation is defined for each distinct librational or rotational domain of the one-degree-of-freedom reduced Hamiltonian $\widehat{h}$:

$$(S, A, \sigma, \alpha) \longmapsto (\mathcal{I}, A', \phi, \alpha') \tag{D.3}$$

such that (A', α') is closed to (A, α), conjugating $\widehat{h}$ to a perturbation of the function (we omit the use of 'primes' for simplicity) $\mathcal{F}(N, \mathcal{I}, A, \alpha)$, which is obtained by expressing the function (D.1) in terms of the adiabatic invariant $\mathcal{I}$ instead of S, σ. Since the Hamiltonian flow of $\mathcal{F}(N, \mathcal{I}, A, \alpha)$ has the constant of motions $\mathcal{I}$, it defines a one-degree of freedom Hamiltonian for the motion of the variables (A, α).

(iii) The adiabatic approximation for the motion of the variables (A, α) given by the Hamiltonian $\mathcal{F}(N, \mathcal{I}, A, \alpha)$ is valid until the system remains within the librational or rotational domain where the adiabatic invariant $\mathcal{I}$ is defined. But the separatrices delimiting such domain may change along time because of the secular variation of the variables (A, α), forcing the system to approach a separatrix. When the motion enters a small neighborhood of the separatrix this adiabatic approximation is no more valid.

(iv) As an example, we refer to Fig. 3 where we represent the phase-portrait of the Hamiltonian $\widehat{h}$ in the (σ, S) plane (top-left panel) as well as the level curves of the adiabatic invariant $\mathcal{I}(N, A, \alpha; h)$ in the secular phase-plane A, α (center panels), computed for a fixed value h of the averaged Hamiltonian and of the action N. In particular, the center-left panel shows the separatrix crossing between region II and region III and the center-right one is related to separatrix crossing between region I and region III. The bold curve is due to the different definition of the adiabatic invariants $\mathcal{I}$ at the two sides of the separatrix.

Appendix E: The Fast Lyapunov Indicator

The Fast Lyapunov Indicators computed in this paper are defined from the variational dynamics of the equations of motions of the non-averaged CR3BP regularized at P_1 with the Kustaanheimo-Stiefel regularization, see Guzzo & lega (2018); Guzzo & Lega (2023); Rossi & Guzzo (2024). Let us denote with: $u \in \mathbb{R}^4$ the KS variables; s the fictitious time related to the physical time by $dt = \|P - P_1\| ds$; $v = du/ds$; $\xi = (u, v)$ the variables of the KS state-space; $w = (w_u, w_v) \in \mathbb{R}^8$ the tangent vector to the space of the variables $\xi = (u, v)$. For any initial datum ξ_0 of the equations of motion of the CRTBP regularized at P_1 with the Kustaanheimo-Stiefel regularization:

$$\frac{d\xi}{ds} = F(\xi), \tag{E.1}$$

and any initial tangent tangent vector w_0, we consider the solution $\xi(s)$ of Eq. (E.1) with initial conditions ξ_0, and the solution $w(s)$ of the variational equations of (E.1):

$$\frac{dw}{ds} = \frac{\partial F}{\partial \xi}(\xi(s))w \tag{E.2}$$

with initial conditions w_0. The regularized Fast Lyapunov Indicator of the initial condition ξ_0, initial tangent vector w_0 and fictitious time T is defined as:

$$FLI(\xi_0, w_0, T) = \max_{0 \le s \le T} \log_{10} \frac{\|w(s)\|}{\|w(0)\|}. \tag{E.3}$$

Appendix F: A reformulation of condition (16)

After some algebraic manipulations of Eq. (14) condition (16) is the solutions A, S of the system:

$$A < 0, \;\; qS - N > 0, \;\; 0 < \frac{S + A}{qS - N} < 1 \tag{F.1a}$$

$$a = (qS - N)^2 \tag{F.1b}$$

$$e = \sqrt{1 - \left[1 - \frac{S + A}{qS - N}\right]^2} \tag{F.1c}$$

$$a(1 - e) < 1. \tag{F.1d}$$

Appendix G: Representation of the Singular Sets

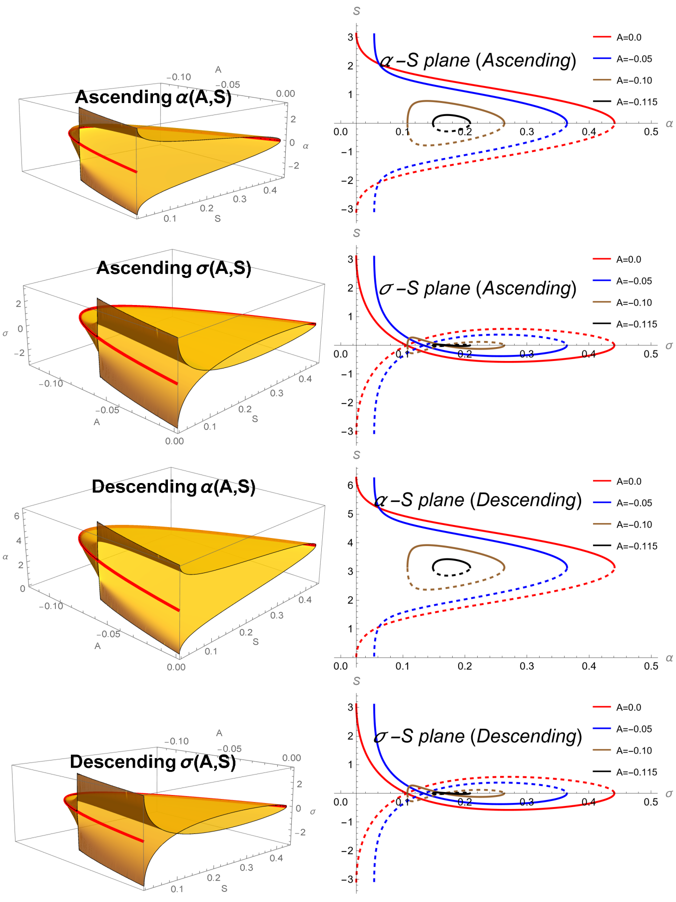

Fig. G.1. Projections of the two branches of the singular set defined by the intersection at the ascending and descending nodes on three and two dimensional subset of variables, for $N = -0.85$. Left panels: three-dimensional illustration of $\sigma = \sigma(S, A, N), \alpha = \alpha(S, A, N)$, respectively. Right panels: representation of the singular set in (S, σ) and (S, α) planes for different values of A. The continuous and dashed curves refer to the value of the index $j = 1, 2$ identifying the two solutions (19) for the ascending node; same notation for the descending node.

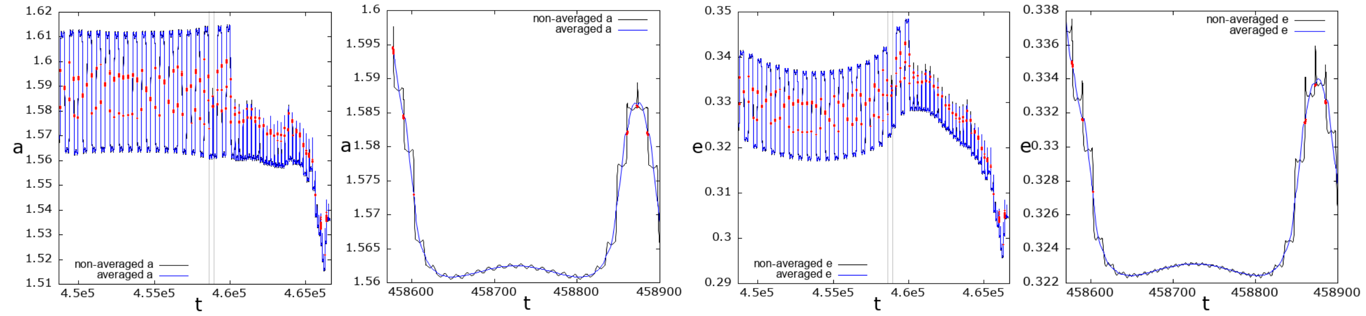

Fig. G.2. Time evolution of the orbital elements a, e before (in black) and after (in blue) the averaging transformation for the orbit analyzed in Fig. 5 (the red dots sample points of the graph for which P has a close encounter with P_1 at a distance smaller than 0.15). The zoom in the second and fourth panels (corresponding to the time interval highlighted with a gray box in the first and third panels) are used to better appreciate the efficacy of the averaging transformation).

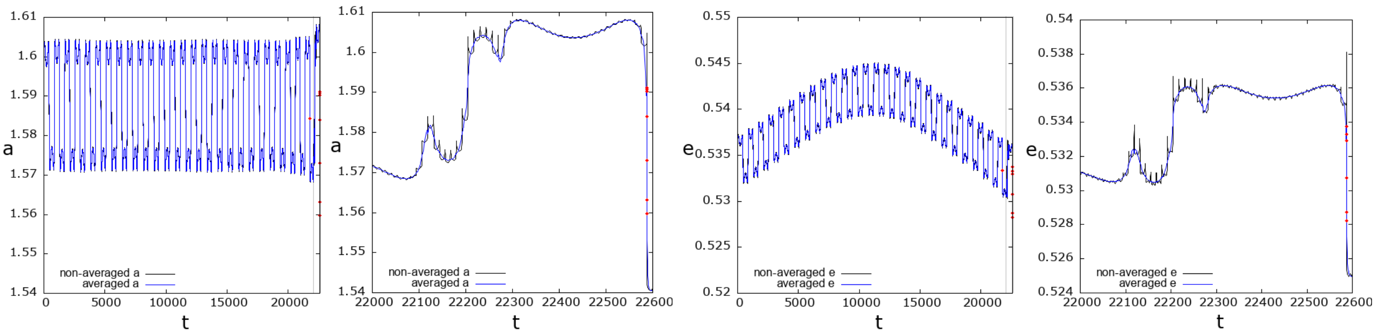

Fig. G.3. Time evolution of the orbital elements a, e before (in black) and after (in blue) the averaging transformation for the orbit analyzed in Fig. 9 (the red dots sample points of the graph for which P has a close encounter with P_1 at a distance smaller than 0.05). The zoom in the second and fourth panels (corresponding to the time interval highlighted with a gray box in the first and third panels) are used to better appreciate the efficacy of the averaging transformation). In the panels of Fig. G.4 we highlight the effects of deeper close encounters occurring on a different zoomed time interval.

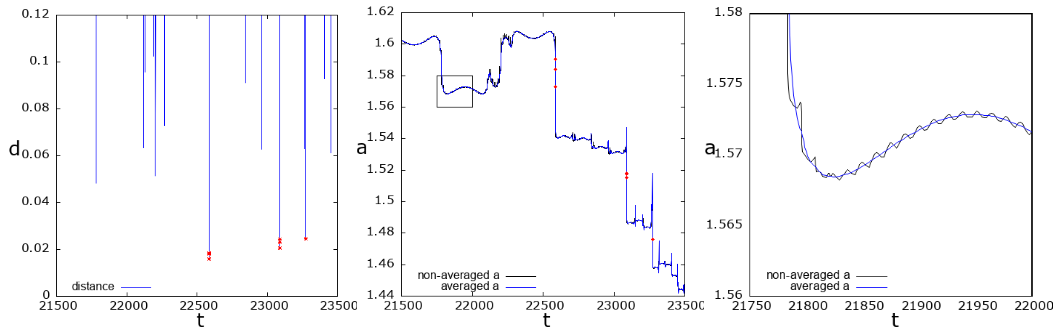

Fig. G.4. Time evolution of the distance of P from P_1 (left panel) and of the value of a (center and right panels) computed before (in black) and after (in blue) the averaging transformation for the orbit analyzed in Fig. 9 and Fig. G.3. We appreciate the efficacy of the averaging transformation in reducing local oscillations of a, except for during the deepest close encounters occurring at a distance smaller than 0.025.

In Fig. G.1 we provide graphical representations of the projection of the singular set on the three-dimensional spaces S, A, σ and S, A, α, for $N = -0.85 > N_c$ (left column). We also represent in the two–dimensional planes S, σ and S, α the curves obtained by fixing the value of A (right column), distinguishing between the intersections occurring at the ascending or descending node and the solutions identified by the two different indices $j = 1, 2$ in Eq. (19) (a similar representation holds for the descending node).

From the panels, we can observe the intricate changes in the points of the singular set, as the values of certain variables changes. The complex patterns of these changes reveal the multifaceted nature of the singular set's structure. For example, let us consider the intersections of the singular set with the plane (S, σ) for fixed values of (A, N, α), with $N = -0.85, A = -0.05$: in the top-right panel the blue curve identifies the values of (S, α) for which $\alpha = \hat{\alpha}(S, A, N)$ (obtained for the ascending node). Therefore, if we fix the value of α, we have one value of $S = S_*$ provided by the solution with $j = 1$ or $j = 2$. If we consider the curve $\sigma = \hat{\sigma}(S, A, N)$ (defined by the same value of j) depicted in the second right-panel from the top for the same value of A, for $S = S_*$ we have one value of σ for which $(S, A, N, \sigma, \alpha)$ is in the singular set. Another point may be found by repeating the procedure for the descending node.